Molecular Determinants of μ-Conotoxin KIIIA Interaction with the Voltage-Gated Sodium Channel Nav1.7

Ian H. Kimball[1,*], Phuong T. Nguyen[1,*], Baldomero M. Olivera[2],

Jon T. Sack[1,‡], Vladimir Yarov-Yarovoy[1,‡]

[1]Department of Physiology and Membrane Biology, UC Davis, Davis, CA, USA,

[2]Department of Biology, University of Utah, Salt Lake City, UT, USA

* - these authors contributed equally to this work

‡ corresponding authors

Abstract

The voltage-gated sodium (Nav) channel subtype Nav1.7 plays a critical role in pain signaling, making it an important drug target. Here we studied the molecular interactions between μ-conotoxin KIIIA (KIIIA) and the human Nav1.7 channel (hNav1.7). We developed a structural model of hNav1.7 using Rosetta computational modeling and performed in silico docking of KIIIA using RosettaDock to predict residues forming specific pairwise contacts between KIIIA and hNav1.7. We experimentally validated these contacts using mutant cycle analysis. Comparison between our KIIIA-hNav1.7 model and the recently published cryo-EM structure of KIIIA-hNav1.2 revealed key similarities and differences between channel subtypes with potential implications for the molecular mechanism of toxin block. Our integrative approach, combining structural data with computational modeling, experimental validation, and molecular dynamics simulations will be useful for engineering molecular probes to study Nav channel function, and for rational design of novel biologics targeting specific Nav channels.

Introduction

Voltage-gated sodium (Nav) channels play a key role in the action potential generation in excitable cells (1-3). The nine subtypes of Nav channel α-subunits (named Nav1.1-Nav1.9) are differentially expressed throughout tissues, and are targets of therapeutics for pain, cardiac arrhythmias, and epilepsy (4). Human Nav1.7 (hNav1.7) is important for pain signaling and its mutations have been linked to severe pain disorders ranging from complete lack of pain sensation to extreme sensitivity to pain (5-7). Clinical use of local anesthetic drugs, such as lidocaine, is limited because they bind to a highly conserved receptor site within the Nav channel pore lumen, and are consequently non-selective among Nav subtypes (8-11). The receptor sites of other Nav blockers have nuanced differences between subtypes, and an atomic-scale understanding of the channel architecture and mechanisms of blockade could enable design of Nav subtype-selective therapeutics (12).

The search for novel Nav channel modulators has identified small disulfide-knotted peptide toxins from cone snails (conotoxins) (13), which target the extracellular vestibule of the Nav channel pore and offer peptide scaffolds for rational design of novel peptide-based therapeutics to treat pain, arrhythmias, and epilepsy (14, 15). μ-conotoxin KIIIA (KIIIA) is a 16 amino acid peptide that potently inhibits TTX-sensitive Nav channels (13, 16, 17), and has analgesic properties in animal models of pain (16) (Figure 1A). KIIIA has variable degrees of affinity and block for the different Nav channel subtypes, with 5 nM affinity for rat Nav1.2, 37 nM for rat Nav1.4, and 97 nM for hNav1.7 (13, 16, 18). Structure-activity relationship studies have identified the KIIIA residues K7, W8, R10, D11, H12 and R14 as key for binding to various Nav channel subtypes (16, 18). Specifically, K7, R10 and R14 have been shown to contribute to both binding affinity and block of hNav1.7 (18). Interestingly, the relative contribution of KIIIA residues in binding to Nav channels vary between channel subtypes. For example, substitution R14A in KIIIA reduces the

affinity for Nav1.2 and Nav1.4 by two orders of magnitude, while only reducing the affinity for Nav1.7 by 5-fold (18). Substitution R10A in KIIIA similarly shows reduced effect on affinity for Nav1.7 compared to Nav1.2 and Nav1.4, while having a more drastic effect on channel block of Nav1.7 (18). In addition, KIIIA blocks Nav channels incompletely and can co-bind with tetrodotoxin (TTX) to TTX-sensitive Nav channels (19).

Previous studies identified the importance of Nav channel residues near the selectivity filter on the P2-helix in domain III (DIII) for their apparent coupling to residues R10 and R14 on KIIIA (18). Notably, the P2-helix in DIII of hNav1.7 has Threonine at position 1398 and an Isoleucine at position 1399, while all other human Nav channels have Methionine and Aspartate at the corresponding positions (18). These residues were proposed to play a role in the selectivity of KIIIA binding to Nav1.2 and Nav1.4 versus to Nav1.7 (18). Molecular modeling of KIIIA binding to rNav1.4 using restraints from experimental data also revealed contacts between KIIIA and the P2-helix in DIII (20). However, these studies did not provide an explanation for the significant effect of the KIIIA mutations H12A, W8A and D11A on toxin affinity.

In this study, we used computational and experimental techniques to investigate the molecular mechanism of the KIIIA interaction with hNav1.7. We present a structural model of KIIIA binding to the hNav1.7 channel based on the eukaryotic electric eel Nav1.4 cryo-EM structure. Our model revealed binding of KIIIA to hNav1.7 at the interface between the P2-helices in domain II (DII) and DIII, which exposed a partially open ion conduction pathway that may explain the incomplete blocking characteristic of the toxin. We identified several unique contacts between KIIIA and extracellular loops on hNav1.7, providing key structural insights into binding specificity for different Nav channel subtypes. We used mutant cycle analysis to validate representative pairwise contacts between specific KIIIA and hNav1.7 residues identified from our structural model of the

KIIIA – hNav1.7 complex. Remarkably, the recently published cryo-EM structure of KIIIA - hNav1.2 complex (21) agrees with findings from our computational modeling and functional study. The high atomic accuracy of peptide toxin – Nav channel interactions modeling with Rosetta in combination with functional testing paves the way for the rational design of novel selective inhibitors targeting Nav channels with high selectivity and potency.

Results

Molecular modeling suggests eccentric binding of KIIIA to DII and DIII of the hNav1.7 pore

To characterize the molecular mechanism of the KIIIA interaction with hNav1.7, we utilized computational modeling and functional validation approaches as described below. When this study was conducted, the cryo-EM structure of the electric eel Nav1.4 (eeNav1.4) (22) channel was the closest structural homolog available to build a homology model of hNav1.7. The eeNav1.4 structure shares ~54% sequence identity with hNav1.7 overall and ~75% sequence identity over the hNav1.7 pore region. We used the RosettaCM modeling approach (23, 24) to generate a structural model of hNav1.7 based on the eeNav1.4 structure (22) and the Rosetta protein-protein docking approach (24-26) to predict a structure of the KIIIA – hNav1.7 complex and identify specific residues forming interactions between KIIIA and hNav1.7 (see Materials and methods, and coordinates of our KIIIA – hNav1.7 model in Supplement File – Model 1). Our model revealed an eccentric binding of KIIIA to hNav1.7, where the KIIIA helical region is positioned perpendicular to the P2-helix in DII with the positively charged KIIIA residues facing the selectivity filter (Figure 1B). Mapping of the open space surrounding the KIIIA - hNav1.7 binding interface revealed a tunnel traversing from the extracellular environment to the channel pore cavity

(Figure 1C). The most constricted part of tunnel is within the selectivity filter region where the radius of the open space drops to ~1 Å. KIIIA bound to the upper region of the selectivity filter and constricted the open space to a minimum radius of ~2.5 Å, which is large enough to allow sodium ion conduction and consistent with the characteristic incomplete block of Nav channels by KIIIA (16, 18). Our KIIIA – hNav1.7 complex model based on eeNav1.4 structure is very similar to our earlier KIIIA – hNav1.7 complex model (27) based on the bacterial NavAb channel structure (PDB: 3RVY (28)) (Figure 1—figure supplement 1A). KIIIA position and orientation in our model is different from KIIIA binding to the P2-helix in DIII previously suggested by computational modeling (18, 20) and lanthanide-based resonance energy transfer (29) studies. Notably, the KIIIA binding just above the selectivity filter in our model is different from TTX and saxitoxin (STX) binding deeper into the selectivity filter region (30, 31).

Pairwise interactions identified from the KIIIA - hNav1.7 complex model

To identify key KIIIA residues at toxin – channel interface, we examined the contribution of KIIIA residues to the interaction with hNav1.7 using an *in silico* alanine scan (see Materials and methods). Non-cysteine residues on KIIIA were mutated to Alanine and changes in Rosetta binding energy ($\Delta\Delta G$) were reported in the arbitrary Rosetta Energy Unit (R.E.U). Our analysis revealed the active surface of KIIIA where residues K7, W8, R10, H12, and R14 each have significant contribution to the binding energy (Figure 1D and E). K7, W8, R10, and H12 are located on the same face of KIIIA's alpha helix, while R14 is located within the C-terminal tail region. Our KIIIA – hNav1.7 model predicts that positively charged residue K7 forms a salt bridge with E919 on the P2-helix in DII (we use hNav1.7 residue numbering throughout the manuscript unless otherwise noted) (Figure 1F). In addition, W8 and H12 were shown to form hydrogen

bonds with Y339 on the extracellular loop between S5 and the P1-helix (S5P1) in DI and D923 on the P2-helix in DII, respectively (Figure 1F). D11 is positioned near the interface between the P2-helices in DII and DIII and forms hydrogen bonds with both K7 on KIIIA and T1398 on the P2-helix in DIII (Figure 1F). The other positively charged KIIIA residues, R10 and R14, interact with two negatively charged residues: D1662 on the extracellular loop S5P1 in DIV and E1417 on the extracellular loop between the P2-helix and S6 (P2S6) in DIII. Notably, R14 also interacts with Y1416 on the extracellular P2S6 loop in DIII and contributes to a cation-π interaction tower formed by Y1402 on the P2-helix in DIII, R896 on the extracellular loop S5P1 in DII, and Y1416 (Figure 1F). This position of R14 is different from the previously proposed proximity between R14 and D1241 on the P2-helix in DIII of rat Nav1.4 (18) (corresponding to I1399 in hNav1.7). However, the R10 position in proximity to I1399 on the P2-helix in DIII is in agreement with previously reported the significant coupling energy between R10 and D1241 on the P2-helix in DIII in rNav1.4 (18). We also observed the interaction between KIIIA N3 and E307 in the extracellular loop S5P1 in DI but this interaction may not be substantial as it is fully exposed in the bulk solvent, as shown by minimal change in Rosetta binding energy ($\Delta\Delta G$) from our *in silico* alanine scan (Figure 1D). Indeed, N3 has been shown to be not critical for KIIIA interaction with rNav1.2 and rNav1.4 (16).

Functional mapping of KIIIA residues at the toxin – channel interface supports the model

To characterize the accuracy of our KIIIA – hNav1.7 model, we first tested the activity of the wild-type KIIIA on the wild-type hNav1.7 using whole-cell voltage-clamp recordings. At the highest KIIIA concentration tested (10 μM) we observed up to ~90% inhibition of sodium current (Figure 2A), in agreement with previous studies concluding that Nav channels retain 5-10% of their

conductance when blocked by KIIIA (16, 18). To estimate the KIIIA binding affinity, we performed concentration-response experiments and obtained an IC_{50} of 410±160 nM and 95% maximal block (Figure 2B,C), which is 4-fold higher than the K_d of 97 nM previously reported for hNav1.7 (18). In our tests, the dissociation rate constant, k_{off}, for the wild-type KIIIA from the wild-type hNav1.7 (0.003 min^{-1}) (Figure 2A, Table 1) was 6-fold slower than previously reported the k_{off} of 0.017 min^{-1} (18). The extremely slow dissociation of the wild-type KIIIA from hNav1.7 complicated accurate determination of dissociation kinetics, as less than 10% recovery was observed during wash-off experiments lasting up to ~30 min. Constraining single exponential fits of the dissociation data to assume maximum recovery, we obtained k_{off} between 0.002 min^{-1} and 0.005 min^{-1}. An upper limit of k_{off} was estimated from the extrapolation of a linear rate of recovery from these experiments providing a k_{off} of 0.003 min^{-1} and a K_d of 59 nM, which is closer to the previously reported K_d of 97 nM (18). Temperature differences between our experiments (~21ºC) and previously published experiments (~25ºC) (18) might be responsible for the slower kinetics. Although we note differences in rates and calculated affinities, overall the activity of the wild-type KIIIA on hNav1.7 in our experiments was similar to previously reported data (18).

We performed an alanine scan of KIIIA residues that are positioned at the interface with hNav1.7 in our model. KIIIA substitutions K7A and H12A both had nearly 100-fold decrease in affinity for the wild-type hNav1.7 channel, in agreement with previously published data (16, 18, 19). From the residues we tested, only K7A had a major effect on block, with reduction of maximal block by 20% (Figure 2C). We found that KIIIA substitutions W8A and D11A had a 50- and 10-fold reduction in affinity for the wild-type hNav1.7 channel, respectively (Figure 2D). For most KIIIA point mutations, the association rate remained similar to wild-type KIIIA, with only D11A showing a modest 3-fold increase in association rate (Figure 2D). The change in affinity was

largely driven by between 36- and 116-fold increases in toxin dissociation from neutralizing mutations for the basic KIIIA residues tested (Figure 2D). Kinetic data for k_{on}, k_{off}, K_d, and calculated fractional block at saturating concentration (F_{block}) are summarized in Table 1 and representative data are shown in Figure 2—figure supplement 1A. The KIIIA-D11A substitution resulted in both an increase in k_{on} and k_{off} and the potential removal of a contact with T1398 on the P2-helix in DIII observed in our model. Prior studies had observed that the D11A substitution had no effect on dissociation from rNav1.2, but had a small effect on rNav1.4 binding—increasing k_{off} 4-fold and very little effect on k_{on} (16). The reductions in KIIIA affinity from alanine mutations seen *in vitro* do not scale in magnitude with the *in silico* R.E.U. ΔΔG values, but do correctly identify residues forming the KIIIA-hNav1.7 interface. Together these results support the toxin – channel interface observed in our model; with the alpha helical portion of the toxin making close contact with the channel and the toxin N- and C-termini facing out (Figure 1B).

Table 1

Kinetics of toxin variants binding to WT-hNav1.7 from whole-cell voltage-clamp. experiments

Fractional block at saturating concentrations determined from extrapolation from kinetic data.

Channel and Toxin (n)	k_{on} **($\mu M^{-1}min^{-1}$)**	***SEM***	k_{off} **(min^{-1})**	***SEM***	K_d **(μM)**	***SEM***	F_{block}	***SEM***
WT-hNav1.7 x WT-KIIIA (5)	0.054	0.011	0.003	0.001	0.059	0.007	0.95[a]	0.033
WT-hNav1.7 x KIIIA-K7A (5)	0.064	0.018	0.274	0.012	4.291	1.507	0.74	0.049
WT-hNav1.7 x KIIIA-W8A (3)	0.110	0.045	0.329	0.097	2.990	1.719	0.90	0.094
WT-hNav1.7 x KIIIA-D11A (4)	0.164	0.014	0.109	0.008	0.663	0.056	1.00	0.012
WT-hNav1.7 x KIIIA-H12A[b] (5)	0.047	0.027	0.349	0.240	7.405	2.801	*0.88*	-

a – Fractional block was determined from the Hill fit of concentration-response data (Figure 2B).

b – Fractional block reported by McArthur, et al., 2011(18) was used to constrain kinetic parameter estimates from association experiments.

n – number of cells tested.

Functional mapping of hNav1.7 residues at the toxin – channel interface support toxin orientation

To identify the key residues forming the KIIIA receptor site on hNav1.7, we originally selected mutations in the P2-helices in DI and DII in the outer pore based on an earlier KIIIA – hNav1.7 model (27) based on the bacterial channel NavAb (PDB: 3RVY (28)) (Figure 1—figure supplement 1A), which was later superseded by our current KIIIA – hNav1.7 model (32) based on eeNav1.4 structure (22) shown in Figure 1. Notably, our earlier and current KIIIA – hNav1.7 models have the same hNav1.7 residues in the P2-helices in DI and DII interacting with KIIIA. We tested the N365 and Y362 residues on the P2-helix in DI and E919 and D923 on the P2-helix in DII. We selected these residues to inform the accuracy of the orientation of KIIIA in our model (Figure 1F). The E919A mutation did not produce measurable current, but the E919Q mutation produced functional currents and reduced binding of the wild-type KIIIA by 42-fold (Figure 2E). The D923A mutation reduced affinity of the wild-type KIIIA by 40-fold (Figure 2E). N365A showed normal block and increased toxin association, yet slowed k_{off} such that dissociation was not measurable during the course of our wash-out experiments (Table 2). Y362C produced a modest increase in both association and dissociation yielding a 7.5-fold reduction in affinity (Figure 2E). This residue is of particular importance in TTX binding (33) and reduced the predicted maximal block by the wild-type KIIIA by ~20% (Figure 2C). Overall, hNav1.7 mutations E919Q,

D923A, and Y362C reduce the binding of the wild-type KIIIA to hNav1.7 in agreement with our structural model of KIIIA – hNav1.7 complex and recent KIIIA – hNav1.2 structure (21). The effect seen by mutations E919Q and D923A in the P2-helix in DII are consistent with the direct interactions suggested from our model (see representative data in Figure 2—figure supplement 1B).

Table 2

Effects of hNav1.7 mutation on WT-KIIIA binding kinetics from whole-cell voltage-clamp experiments

Fractional block at saturating concentrations determined from extrapolation from kinetic data.

Channel and Toxin (n)	k_{on} ($\mu M^{-1}min^{-1}$)	*SEM*	k_{off} (min^{-1})	*SEM*	K_d (μM)	*SEM*	F_{block}	*SEM*
WT-hNav1.7 x WT-KIIIA (5)	0.054	0.011	0.003	0.001	0.059	0.007	0.95[a]	0.033
Y362C x WT-KIIIA (3)	0.101	0.016	0.044	0.004	0.436	0.052	0.75	0.055
N356A x WT-KIIIA (2)	0.086	0.006	n.d.	-	n.d.	-	n.d.	-
E919Q x WT-KIIIA (3)	0.040	0.003	0.101	0.003	2.51	0.16	0.92	0.028
D923A x WT-KIIIA (3)	0.083	0.022	0.193	0.022	2.34	0.41	0.89	0.037

a – Fractional block was determined from the Hill fit of concentration-response data (Figure 2B)

n – number of cells tested.

Double Mutant Cycle Analysis confirms pairwise interactions between KIIIA and hNav1.7-DII

In our single mutagenesis experiments we found strong support for the hypothesized toxin-channel interface observed in our model and the KIIIA - Nav1.2 structure, yet these experiments could not

validate specific pairwise toxin – channel contacts. To further validate our KIIIA – hNav1.7 model, we performed double-mutant experiments (34) isolating the contributions of specific pairwise contacts to the binding energy between KIIIA and hNav1.7 (Figure 3). In examining cycles of KIIIA substitutions at positions K7 and D11 with hNav1.7 E919Q, and KIIIA H12 with Nav1.7 D923A, we compared the effects of single mutations to those of double mutations (Figure 3A and Figure 3—figure supplement 1). Pairwise contacts can be identified on the basis of the path-independence from the wild-type condition to the double-mutant condition: the reduction in binding energy resulting from a mutation to either side of an interacting pair should be non-additive in the double-mutant condition (34). Residue pairs that exhibit additive effects of the double-mutant relative to the single mutants would be expected to make little functional interaction contributing to the binding energy. These effects are quantified by calculating the coupling coefficient Ω, and the coupling energy $E_{coupling}$ = -RTlnΩ (see Materials and methods). Strongly interacting residue pairs will have Ω values significantly different from 1.0, while non-interacting pairs will trend towards Ω values close to 1.0 (34). Importantly, while strongly interacting pairs are expected to show coupling, an apparent coupling can result from allosteric effects, and can also be influenced by the particular mutations used to eliminate the proposed interaction. We tested the following pairs of double mutants: E919Q x K7A, D923A x H12A (Figure 3—figure supplement 1), which both interact directly in our model (Figure 4A), and E919Q x D11A, which do not interact directly in our model, with the hypothesis that the interacting pairs will exhibit large $E_{coupling}$. E919Q x D11A greatly reduced the toxin affinity (K_d =14.2±5.8 μM) relative to either of the single mutations, E919Q and D11A (2.34±0.16 μM and 0.66±0.06 μM, respectively) (Figure 3B and Table 3), with Ω = 0.5 and $E_{coupling}$ = 0.4±0.19 kcal·mol^{-1}, suggesting a weak interaction and supporting the separation of these residues in our model (Table 4) (35, 36). For E919Q and

K7A, the double mutant showed similar binding affinity (2.47±1.32 μM to the channel mutation alone (2.51±0.16 μM), while both had a lower affinity than the K7A variant on the wild-type channel (4.29±1.51 μM) (Figure 3A and Table 3). This corresponded to a strong coupling between E919Q and K7A (Ω=0.014 and $E_{coupling}$=2.51±0.23 kcal·mol^{-1}) (Table 4). Likewise, the D923A mutation reduced the affinity of KIIIA (2.34±0.41 μM), but did not show an additive effect with H12A (2.40±1.45 μM) (Figure 3A and Table 3) resulting in significant coupling between D923A and H12 (Ω=0.008 and $E_{coupling}$=2.81±0.24 kcal·mol^{-1}) (Table 4). The large coupling energies observed between these pairs are consistent with strong pairwise interactions between charged amino acids (36). These results are consistent with E919 – K7 and D923 – H12 pairwise interactions observed in both our model (Figure 4A) and the recent structure of KIIIA - Nav1.2 complex (21), which both show strong electrostatic interactions between these residue pairs, providing further experimental validation of the KIIIA binding pose observed in our model.

Table 3

Kinetics of double-mutant cycle pairs from whole-cell voltage-clamp experiments.

Fractional block at saturating concentrations determined from extrapolation from kinetic data.

Channel and Toxin (n)	k_{on} (μM^{-1}min^{-1})	***SEM***	k_{off} (min^{-1})	***SEM***	K_d (μM)	***SEM***	F_{block}	***SEM***
WT-hNav1.7 x WT-KIIIA (5)	0.054	0.011	0.003	0.001	0.059	0.007	*0.95*[a]	0.033
WT-hNav1.7 x KIIIA-K7A (5)	0.064	0.018	0.274	0.012	4.29	1.51	0.74	0.049
WT-hNav1.7 x KIIIA-D11A (4)	0.164	0.014	0.109	0.008	0.66	0.056	1.00	0.012
WT-hNav1.7 x KIIIA-H12A*[b] *(5)	0.047	0.027	0.349	0.240	7.40	2.80	*0.88*	-

E919Q x WT-KIIIA (3)	0.040	0.003	0.101	0.003	2.51	0.16	0.92	0.028
E919Q x KIIIA-K7A (3)	0.044	0.015	0.108	0.021	2.47	1.32	0.48	0.066
E919Q x KIIIA-D11A (3)	0.124	0.046	1.790	0.369	14.2	5.79	*0.92*[c]	-
D923A x WT-KIIIA (3)	0.083	0.022	0.193	0.022	2.34	0.41	0.89	0.037
D923A x KIIIA-H12A (2)	0.183	0.065	0.440	0.098	2.40	1.45	0.49	0.092

a – Fractional block was determined from the Hill fit of concentration-response data (Figure 2B).

b – Fractional block reported by McArthur, et al., 2011(18) was used to constrain kinetic parameter estimates from association experiments.

c – Fractional block from E919Q mutation assumed to constrain kinetic parameter estimates from association and dissociation based on lack of effect on block by D11A variant.

n – number of cells tested.

Table 4

Coupling coefficients and coupling energies from double-mutant cycle experiments

	D923A x H12A	***Error***	***E919Q x K7A***	***Error***	***E919Q x D11A***	***Error***
$E_{coupling}$ **kcal·mol** $^{-1}$	*2.81*	*0.24*	*2.51*	*0.23*	*0.40*	*0.19*
1 / Ω	*122*	*61*	*74.0*	*35*	*2.00*	*0.76*

Error calculated by linear propagation of uncertainty.

Divergent channel sequence contributes to KIIIA binding specificity for Nav channel isoforms

The differences in KIIIA binding affinity between the Nav channel isoforms likely arises from variations in sequence within the toxin binding site (Figure 4A and B). The recent structure of the

KIIIA - hNav1.2 complex (21) supports the predictions from our structural model of the KIIIA - hNav1.7 complex. The backbone root mean square deviation (RMSD) of the KIIIA - hNav1.7 model and the KIIIA - hNav1.2 structure over KIIIA and the P2-helices is ~1.0 Å (Figure 1—figure supplement 1B). The specific pairwise contacts between K7-E919 and H12-D923 in our KIIIA - hNav1.7 model, validated by mutant cycle analysis, are in agreement with the corresponding pairwise contacts between K7-E945 and H12-D949 observed in the KIIIA - hNav1.2 complex structure (Figure 4A and B) (21). Our KIIIA - hNav1.7 model also correctly predicted other non-tested contacts homologous to those observed in the published structure, including pairwise interactions between KIIIA N3 and W8 with E307 and Y339, respectively, on the extracellular S5-P1 loop in DI (Figure 4A and B).

Interestingly, the KIIIA residues D11 and R10 in our KIIIA - hNav1.7 model are positioned similarly in the KIIIA - hNav1.2 structure, but details of toxin – channel interactions involving these residues are different (Figure 4A). D11 forms a hydrogen bond with T1398 on the P2-helix in DIII in our KIIIA - hNav1.7 model (Figure 4A), but the substitution of Thr (T1398) hNav1.7 to Met (M1425) on the P2-helix in DIII in hNav1.2 removes this interaction and a new hydrogen bond is formed with the nearby residue Y1429 (Figure 4—figure supplement 1) (21). Residues T1398 and I1399 on the P2-helix in DIII of hNav1.7 are Met and Asp, respectively, in all other human Nav channels. In the hNav1.2 structure, R10 interacts with D1426 on the P2-helix in DII, but the corresponding position in hNav1.7 is I1399, eliminating possible charge interaction with this residue in hNav1.7 (Figure 4A and B). This difference potentially contributes to the R10 interaction with the nearby acidic residue D1662 on the extracellular S5-P1 loop in DIV of hNav1.7 (Figure 4—figure supplement 1). Notably, Asp at position 1662 is unique to hNav1.7 -

corresponding residues at this position in other Nav channel subtypes are Val, Ala, and Ser (Figure 4B).

Several additional positions on the extracellular loop regions of Nav channels may also contribute to specific interactions between KIIIA and Nav channels. Both our KIIIA - hNav1.7 model and the KIIIA - hNav1.2 structure show the positively charged R14 forming cation – π interactions with Y1416 (hNav1.7) or Y1443 (hNav1.2) on the extracellular P2-S6 loop in DIII (Figure 4A). Notably, in the KIIIA - hNav1.2 structure R14 is also in proximity to the negatively charged E919 (hNav1.2 numbering) on the extracellular S5-P1 loop in DII (21). However, in our KIIIA - hNav1.7 model R14 is in proximity to T893 on the extracellular S5-P1 loop in DII (which is corresponding to E919 in hNav1.2) and E1417 on the extracellular P2-S6 loop in DIII (Figure 4A and B). These sequence and structural differences might be responsible for the reported KIIIA R14A mutant selectivity for hNav1.7 versus hNav1.2 (18). Thus, despite the overall similarity in binding pose and channel architecture, sequence differences between hNav1.7 and hNav1.2 at KIIIA binding site contribute to specific differences in toxin – channel interactions between our KIIIA - hNav1.7 model and the KIIIA - hNav1.2 structure.

Differences in structural dynamics of KIIIA binding to hNav1.7 and hNav1.2 revealed by molecular dynamics simulations

To further study the molecular mechanism of the KIIIA interaction with hNav1.7, we performed a molecular dynamics (MD) simulation of our KIIIA - hNav1.7 complex model, as described in Materials and methods. The 1μs simulation revealed relatively stable binding of KIIIA within the

receptor site with notable dynamics of specific KIIIA residues. During the simulation, the RMSD of hNav1.7 at the interface between KIIIA and hNav1.7 was ~4Å (Figure 5A). After equilibration, the sodium ion in the selectivity filter is localized at E916 and E919 on the P1-P2-helix region in DII (A1 configuration, Figure 5A). This agrees with the density identified as a sodium ion at the same position in the cryo-EM structure of the KIIIA - hNav1.2 complex. In our MD simulation, this sodium ion diffused out to the extracellular bulk via an open passage formed between KIIIA and the channel. The sodium ion escape is consistent with the incomplete block of Nav current observed in experiments (Figure 2) due to incomplete elimination of the unitary conductance of Nav channels when KIIIA is bound (16, 18). After the escape of the sodium ion from the selectivity filter, the KIIIA - hNav1.7 structure relaxed in this configuration for about 100 ns (A2 configuration, Figure 5A) and then dynamically changed towards a slightly different binding configuration in which K7 on KIIIA formed interactions with Y362 and E364 on the P2-helix in DI, and D1690 on the P2-helix in DIV (A3 configuration, Figure 5A). This agrees with our functional characterization of KIIIA - hNav1.7 interactions where we observed a 100-fold reduction in K_d for the K7A mutation on KIIIA and only a 42-fold reduction for E919Q mutation on the channel, a mutation that may not completely disrupt the interaction at position 919 with K7. R10 is still neighboring I1399 on the P2-helix in DIII and switched from interacting with D1662 on the extracellular S5-P1 loop in DIV to interacting with D1690 on the P2-helix in DIV (Figure 5A and C, Video 1). Interestingly, with both K7 and R10 reaching towards the P2-helix in DIV during the MD simulation, the channel appeared to be more completely blocked in this configuration (Figure 5—figure supplement 1A and B). In addition, we also observed dynamic coupling of other key residues on KIIIA with the P2-helices and extracellular loop regions of hNav1.7 (Figure 5A). W8 interacted with K310 and Y339 on the extracellular S5-P1 loop in DI.

H12 showed significant interactions with D923 on the P2-helix in DII and also with the backbone of P895 on the extracellular S5-P1 loop in DII. D11 is positioned deep at the interface between DII and DIII formed by W897 on the extracellular S5-P1 loop and E919 in the P2-helix in DII and T1398 and Y1402 on the P2-helix in DIII. R14 primarily interacted with Y1416 on the extracellular P2-S6 loop in DIII and did not maintain interaction with E1417 on the extracellular loop in DIII as identified in our model. Notably, R14 also formed interactions with T893, L894, and P895 on the extracellular S5-P1 loop in DII (Figure 5A and Figure 5—figure supplement 2).

The recently published cryo-EM structure of KIIIA - hNav1.2 complex allowed us to investigate its structural dynamics and compare them to dynamics observed in our KIIIA - hNav1.7 complex model (Figure 5A). We used the same simulation procedure as previously applied for the KIIIA - hNav1.7 model (see Materials and methods). Similarly, our simulation revealed relatively stable binding of KIIIA within the receptor site of hNav1.2 with notable dynamics of specific KIIIA residues. During the simulation, the RMSD of the hNav1.2 at the interface between KIIIA and hNav1.2 was ~4Å (Figure 5B). The sodium ion in the selectivity filter, identified from the structure, at the site formed by E942 and E945 (corresponding to E916 and E919 in hNav1.7) on the P1-P2-helix region in DII of hNav1.2 quickly diffused out to the extracellular bulk, in agreement with an incomplete block by KIIIA (16) and our simulation of the KIIIA - hNav1.7 model (Figure 5A and B). In contrast to our KIIIA – hNav1.7 simulation, after the escape of the sodium ion, we did not observe the transition of K7 to form interactions with E387 on the P2-helix in DI and D1717 on the P2-helix in DIV. Instead, K7 formed more stable interactions with E945 and D949 on the P2-helix in DII, and also with N361, Y362 on the extracellular S5-P1 loop in DI (Figure 5B and C). In contrast to the KIIIA - hNav1.7 simulation, R10 stably interacted with D1426

on the P2-helix in DIII (Figure 5B and C) and did not form new interactions with D1717 on the P2-helix in DIV (Video 2). This configuration of K7 and R10 promoted a slight rotation of the KIIIA helical region around the principal axis towards DIII and allowed other key residues to make new interactions with hNav1.2 (Figure 5B and C). Aside from Y362, W8 also interacted with N333, N361, and Y362 in the DI loops and N916 in the DII loop. Interestingly, H12 mainly interacted with Y362 on the extracellular S5-P1 loop in DI, S915 and backbone of I914 on S5-P1 loop in DII. D11 slightly shifted towards the P2-helix in DII and interacted with Y362 on the extracellular S5-P1 loop in DI and E945 on the P2-helix in DII. Similar to the KIIIA - hNav1.7 simulation, R14 stably interacted with Y1443 on the extracellular P2-S6 loop in DIII as well as E919, L920 and the backbone of R922 on the extracellular S5P1 loop in DII (Figure 5B and Figure 5—figure supplement 3).

The dynamics of K7 and R10 in these MD simulations highlight several intriguing differences in the activity of KIIIA against hNav1.7 and hNav1.2 . Notably, D1426 on the P2-helix in DIII of hNav1.2 is conserved among all human Nav channel isoforms, except for hNav1.7, which has I1399 at this position (Figure 4). The absence of Asp at the 1399 position in hNav1.7 allowed the transition of R10 to interact with the nearby acidic residue D1690 on the P2-helix in DIV, and also promoted interaction of K7 with E364 and D1690 that appeared to create a more complete block of the channel as observed in the KIIIA - hNav1.7 simulations, but not in the KIIIA - hNav1.2 simulation (Figure 5—figure supplement 1). Indeed, functional studies showed that the mutation of Asp to Ile in Nav1.4 (D1241) at position corresponding to I1399 in hNav1.7 increased the fractional block, while the reversed substitution of Ile to Asp in Nav1.7 decreased the fractional block (18). In addition, R10A produced a 35% reduction in KIIIA block of rNav1.4, while the loss

of toxin block caused by the R10A mutation was largely rescued by hNav1.7-like Ile in the P2-helix in DIII (18). Combined, these results reveal a structural basis for differences in molecular determinants of KIIIA binding to hNav1.7 versus other Nav channel isoforms driven by sequence variability at key sites surrounding the channel pore.

Discussion

Our computational model of hNav1.7, docking of KIIIA to the hNav1.7 model, and functional testing of KIIIA and hNav1.7 mutations presented here were completed prior to the publication of KIIIA - hNav1.2 complex structure (21). Overall, our KIIIA - hNav1.7 model agrees with the KIIIA - hNav1.2 complex structure. While hNav1.7 and hNav1.2 channels share sequence homology within most of the KIIIA binding region, they exhibit several key differences at the toxin - channel interface. Our model predicted and we functionally characterized specific pairwise contacts between KIIIA and hNav1.7, particularly K7 on KIIIA and E919 on the P2-helix in DII and also H12 on KIIIA and D923 on the P2-helix in DII. These pairwise interactions agree with the corresponding pairwise interactions between K7-E945 and H12-D949 observed in the KIIIA - hNav1.2 complex structure (Figure 4A and B) (32). The similarity between our KIIIA – hNav1.7 model and the KIIIA – hNav1.2 structure highlights the predictive power of our structural modeling and functional testing approach with potential future applications to study other peptide toxin – channel interactions.

Our MD simulations reveal dynamics at the KIIIA – Nav channel interface that occur when KIIIA is bound to hNav1.7 or hNav1.2 that were not observed in the static structures. Notably, the

transitions to a slightly different KIIIA binding configuration in both KIIIA - hNav1.7 and KIIIA - hNav1.2 MD simulations occurred after escape of the sodium ion from the selectivity filter region. It is possible that presence or absence of sodium ion in the selectivity filter may affect the precise KIIIA binding configuration. Further simulations and testing are required to elucidate the role of sodium ion in channel block.

Cryo-EM structures of hNav1.2, hNav1.4, and hNav1.7 channels (21, 30, 37) revealed that the extracellular vestibule of the channel pore targeted by KIIIA is surrounded by several relatively long loop regions, raising the possibility that the access pathway to the KIIIA binding site is relatively narrow. Restricted access and escape pathways for KIIIA binding could confer the relatively slow k_{on} and k_{off} rates observed in our functional studies (Figures 2 and 3) and previously published data (13, 16, 18). We speculate that differences in the external vestibule loops, and the ability to form varied contacts once occupying the binding site could underlie the differences in dissociation rate observed for KIIIA when targeting different Nav channels.

We have demonstrated a combined Rosetta computational modeling, functional characterization, and MD simulations approach to study molecular determinants of toxin – channel interactions. Establishing successful predictions with computational modeling at atomic accuracy is a critical step towards computational design of efficacious novel peptide-based therapeutics. Our results can be potentially expanded to rational design of novel peptides to target the selectivity region of Nav channels. Despite the high sequence conservation in the pore region of Nav channels, our work shows that the specific sequence differences between Nav channels in the extracellular loop regions and the P2-helices of the pore can have large functional consequences on toxin action.

Protein design and optimization informed by these insights could create high-affinity and specificity peptide inhibitors of Nav channels, forming a new class of biologics to treat Nav channel related diseases.

Conclusions

We generated a structural model of the conotoxin KIIIA in complex with hNav1.7 using homology modeling and docking simulations. Our model was validated with functional testing, using alanine-scan mutagenesis of KIIIA and hNav1.7, double mutant cycle analysis of specific pairwise toxin – channel interactions, supporting that acidic residues E919 and D923 on the P2-helix in DII of Nav1.7 contribute significantly to toxin – channel interaction, and that KIIIA forms multiple interactions with the extracellular loops in DI-III. The recently published structure of the KIIIA - hNav1.2 complex further supports predictions observed in our model. Unbiased MD simulations of KIIIA - hNav1.7 and KIIIA - hNav1.2 complexes suggest a potential important role of I1399 on the P2 helix in DIII of hNav1.7 that may underlie the structural basis of KIIIA block of hNav1.7 conductance. Overall, our results further characterize the molecular determinants of the KIIIA interaction with human Nav channels and can be potentially useful for rational design of novel peptide-based therapeutics and for engineering of molecular probes to study Nav channels function.

Acknowledgements

We would like to thank Drs. Heike Wulff, Jie Zheng, and Igor Vorobyov, and members of Yarov-Yarovoy and Sack laboratories for helpful discussions. We thank Dr. Nieng Yan (Princeton

University) for independent comparison of our KIIIA – hNav1.7 model to coordinates of KIIIA – hNav1.2 structure (21) prior to release in Protein Data Bank, and sharing the coordinates of electric eel and human $Na_V1.2$ channel structures. We thank Dr. Christoph Lossin (University of California, Davis) for providing the hNav1.7 cell line and WT-hNav1.7 channel construct, as well as Dr. William Catterall (University of Washington) for the tsa201 cell line. Anton 2 computer time was provided by the Pittsburgh Supercomputing Center (PSC) through Grant R01GM116961 from the National Institutes of Health. The Anton 2 machine (38) at PSC was generously made available by D.E. Shaw Research. This research was supported by U.S. National Institutes of Health awards U01HL126273 and R01HL128537 to VYY, R01NS096317 to JTS, UC Davis Academic Senate Award FL18YAR to VYY, NIH T32 GM099608 to IHK, and AHA 17PRE33670204 to IHK.

Materials and methods

Homology modeling of hNav1.7 based on EeNav1.4 structure

The cryo-EM structure of the Nav1.4-β1 complex from the electric eel (eeNav1.4) (PDB ID: 5XSY) (22) was used to generate the model of hNav1.7 channel using Rosetta structural modeling software (23, 24). Initially, we refined the published coordinates of eeNav1.4, without the β1 subunit by using the Rosetta cryo-EM refinement protocol (39) and picked the lowest scoring density-refitted eeNav1.4 model to use as a template. The comparative modeling protocol RosettaCM (23) was then used in combination with the electron density of the eeNav1.4 to model the hNav1.7 structure. We generated 5,000 structural models of hNav1.7 and selected the top 500 lowest-scoring models for clustering analysis as described previously (40). Visual inspection of the top scoring clustered models was used to select the final model for the docking study.

Molecular docking of KIIIA to the hNav1.7 model

The solution NMR structure of KIIIA (PDB ID: 2LXG) (17) was used as an ensemble to dock to the hNav1.7 model using the RosettaScript XML scheme (24, 41). We initially discovered it is challenging for Rosetta to move the KIIIA structures to pass the narrow passage created by the extracellular loops to fully sample the binding site. We subsequently divided the docking protocol into two stages (see details of Rosetta commands and scripts in Supplementary File 1). In stage 1, docking was performed with the DI S5P1 and DIII S5P1 loops truncated, and full random translational and rotational perturbation of KIIIA at both low and high-resolution phases. This stage generated 20,000 structural models of the docking complexes. We then selected the top 1,000 models based on the total scores and filtered based on the Rosetta $\Delta\Delta$G (an estimate of the binding

energy of a complex) to select the top 500 models. $\Delta\Delta G$ is computed by taking the difference of the energy of the KIIIA – hNav1.7 complex and of the separated KIIIA and hNav1.7 structures. We clustered these complexes using the Rosetta legacy clustering application. The center models of top 20 clusters then passed to stage 2 docking. In this stage, positions of KIIIA in the top 20 clusters were used to create 20 different starting docking trajectories with the full structure of hNav1.7 model including all the extracellular loop regions. The full translational and rotational perturbation used in the previous stage was turn off. Instead, only limited local perturbation was allowed in both centroid and full-atom refinement phases. Similar to stage 1, we generated 20,000 structural docking models and filtered based on the Rosetta total score and $\Delta\Delta G$ to select the top 500 models, which were again clustered to finalize the top 5 complexes for visual inspection. The selected docking model presented here (see coordinates of our KIIIA – hNav1.7 model in Supplement File – Model 1) is the only one in the top 5 clusters models that is in agreement with previously published data (16, 18).

Molecular dynamics simulation of KIIIA - hNav1.7 and KIIIA - hNav1.2 complexes

The docking complex of KIIIA - hNav1.7 and the cryo-EM structure of hNav1.2 (PDB ID: 6J8E) were used to setup systems for MD simulations. For the hNav1.2 structure, Rosetta density refinement protocol was applied as described above for the hNav1.7. The missing region on DI extracellular loop was modeled using Rosetta loop modeling. We placed one sodium ion in the selectivity filter and one in the cavity of the channels as initial setup for both simulations. CHARMM-GUI (42) was used to embed the KIIIA - hNav1.7 model and the KIIIA - hNav1.2 structure (PDB ID: 6J8E) in a lipid bilayer of POPC with explicit TIP3P water molecules at a concentration of 150 mM NaCl. CHARMM36 forcefield was used for proteins, lipids, and waters

in both systems. Each system contains approximately of 164,000 atoms. Protonation state is assigned at neutral pH. N-epsilon nitrogen of H12 on KIIIA is protonated instead of N-delta nitrogen as suggested in both the Rosetta model of hNav1.7 – KIIIA and the hNav1.2 – KIIIA structure. The C-terminal of KIIIA is amidated to be consistent with the KIIIA variant used in our experiments.

Equilibrations were run on our local GPU cluster using NAMD version 2.12 (43). After 10,000 steps of steepest descent minimization, MD simulations started with a timestep of 1 fs with harmonic restraints initially applied to protein heavy atoms and some lipid tail dihedral angles as suggested by CHARMM-GUI (42). These restraints were slowly released over 2 ns. Harmonic restraints (0.1 kcal/mol/$Å^2$) were then applied only to protein backbone atoms, and the systems were equilibrated further for 20 ns with a timestep of 2 fs. All bonds to H atoms were constrained using the SHAKE algorithm in order to use a 2 fs timestep. Simulations were performed in NPT ensemble with semi-isotropic pressure coupling to maintain the correct area per lipid, and constant temperature of 303.15 K. Particle Mesh Ewald (PME) method was used to compute electrostatic interactions. Non-bonded pair lists were updated every 10 steps with a list cutoff distance of 16 Å and a real space cutoff of 12 Å with energy switching starting at 10 Å.

We used the Anton 2 software version 1.31.0 for production runs of 1us of each system on the Anton 2 supercomputer. Simulations were performed in the NPT ensemble at 303.15 K A with 2 fs timestep. Non-bonded long-range interactions computed every 6 fs using the RESPA multiple time step algorithm. The multi-integrator algorithm was used for temperature and semi-isotropic pressure coupling and the u-series algorithm was used for long-range electrostatic interactions. A

long-range Lennard-Jones (LJ) correction (beyond cutoff) was not used as was suggested for CHARMM36 lipid force field.

Cell culture, transfection, and preparation

Electrophysiology experiments were performed on transiently transfected tsa-201 cells (gift from William Catterall) and a HEK 293T cell line stably expressing hNav1.7 (gift from Chris Lossin). Cells were grown at 37ºC, 5% CO_2 in DMEM with 4.5g/L D-glucose, L-glutamine, and 110 mg/L Sodium Pyruvate (Gibco cat# 11995-065) with 10% FBS, and 100 units/mL Penicillin/Streptomycin (Gibco cat# 15140-122). The stable cell line was raised in the same conditions with 500 μg/mL G418 as a selection agent. Cells were grown to 70% confluency in 35mm dishes and passaged every 2-3 days for tsa-201 and 3-4 days for the stable-cell line. Cells were washed with divalent-free DPBS (Gibco cat# 14190-144) and dissociated with 0.05% Trypsin-EDTA (Gibco cat# 25300-054) and seeded to fresh dishes with pre-warmed media. tsa-201 cells were transfected via Lipofectamine 2000 24-48 hours prior to experiments with 1 μg pCMV6-SCN9A (gift from Dr. Christoph Lossin) and 0.5 μg pMaxGFP (Lonza) for identification of transfected cells. Mutant constructs were purchased and coding sequences verified by Mutagenex. Prior to experiments, cells were washed with DPBS and dissociated in 1mL Versene (Gibco cat# 15040-066) and scraped from the dishes and transferred to a 14mL conical tube with 3 mL DMEM. They were centrifuged at 1000 x *g* for 2 minutes and resuspended in a microfuge tube in 1mL extracellular solution (described below) with 10 mM D-glucose and rotated at RT until use.

Electrophysiology

Whole-cell voltage-clamp recordings were performed at RT (21-22°C) in an RC-24N recording chamber fixed to a glass coverslip (Warner Instruments), mounted on a Zeiss Axiovert 35 microscope illuminated with a Zeiss HBO 100W AttoArc lamp and filter set for epifluorescent detection of GFP expressing cells. Approximately 40 μL of cell suspension was added to the pre-filled chamber and allowed to adhere to the glass bottomed chamber for 2-10 minutes. Fresh external solution was perfused through the chamber prior to patching. Borosilicate pipettes (1.5 mm OD, 0.86 mm ID, Sutter instruments cat # BF150-86-7.5HP) were pulled to resistances of 1-2 MΩ, fire-polished, coated with Sylgard, and filled with the internal recording solution. GFP expressing cells were patched and signals were amplified with an Axon Axopatch 200-B (Molecular Devices) and acquired with an Instrutech LIH 8+8 ADC board (HEKA). GΩ seals were obtained, and pipette capacitance was corrected for prior to break-in achieved by suction. Access resistance (R_s) was typically 1-4 MΩ. 60%-80% R_s compensation (10 μs lag) and prediction was used to reduce voltage error to less than 10 mV as determined from the product of the peak current and uncompensated R_s. P/5 leak subtraction protocol was used during recording. Signals were pre-filtered with a low-pass Bessel filter at 5 or 10 kHz before digitizing at 20 kHz and recorded with Patchmaster (HEKA, version 2x90.2) on a Windows 7 PC. The solutions were as follows in mM: External 3.5 KCl, 155 NaCl, 10 HEPES, 1 $MgCl_2$, 1.5 $CaCl_2$ adjusted to pH 7.4 with NaOH, and 315 mOsm; Internal: 35 NaCl, 70 CsCl, 50 CsF, 1 EGTA, 10 HEPES adjusted to pH 7.4 with CsOH at 310 mOsm. After break-in, cells were held at -120 mV and tested for stable Na^+ current with depolarizing 35 ms voltage steps to -10 mV from -120 mV collected every 5 s for up to 5 minutes to allow for a stable level of current prior to vehicle addition. Once stable current levels were achieved, 150 μL of vehicle was added to the bath via pipette with displaced

solution removed via an overflow vacuum line. After approximately 5 minutes, whole cell parameters were checked, and toxin (described below) was added via pipette as with vehicle during recording, with vacuum suction removing displaced bath solution. Once apparent block plateaued, whole cell parameters were re-checked, and pulsing resumed. To measure dissociation, gravity fed perfusion with fresh external solution was started at a rate 1-2 mL/min during recording. Cells with stable leak and R_s allowing fitting to a single-exponential function (see below) throughout the experiment were included for analysis.

Toxin preparation

Lyophilized WT-KIIIA was purchased (Alomone labs, Jerusalem, IS), reconstituted in water and stored as 100 μM stock aliquots at -80ºC prior to use. Toxin variants were produced by solid state synthesis as described previously (16) and stored as stock aliquots at -80ºC prior to use. Stock concentrations were checked by 280nm absorbance on a Nanodrop 2000 spectrophotometer (ThermoFisher) with extinction coefficients determined by the ExPASy ProtParam online tool (44). Stock aliquots of toxin were diluted in equal volumes of 2x External solution with 0.2% BSA for working solutions of toxin in vehicle of 1x External solution with 0.1% BSA and further diluted in 1x vehicle to the working concentration. Vehicle for controls were prepared in the same manner.

Modeling and simulation analysis

Structural modeling data were analyzed using Rosetta and rendered using UCSF Chimera (45), VMD (46) was used to analyze MD simulation data. All data were plotted in R using ggplot2 (47).

Tunnel detection for KIIIA block (Figure 1C and Figure 5—figure supplement 1): We used CAVER (version 3.0) (48) to detect tunnels passing by KIIIA. Coordinates of Lys 7 in KIIIA were used as a searching starting point with probe_radius 0.9, shell_radius 5.0, shell_depth 4.0 and max_distance 10. Multiple tunnels were detected for the whole structures. We visually select only tunnels that have maximum radii greater than 2 and neighboring KIIIA for presentation.

Fractional contacts (Figure 5): Fractional contact is defined as probability of finding two residues, one on the KIIIA and one on the channel forming contacts over time course of simulation. We considered two residues are in contact if any heavy atoms of one residue is within 4 Å of any heavy atoms of the other residues. Only contacts that have probability greater than 0.2 are shown for clarity.

Interface RMSD (Figure 5): We used 10 Å as a cutoff for interface calculation between KIIIA and the channels. The interface is comprised of the KIIIA itself and channel residues that are within 10 Å of KIIIA heavy atoms, defined at the beginning of the simulations. Backbone heavy atoms of the interface were used for RMSD calculation.

Electrophysiology analysis

Electrophysiology data were analyzed and plotted in IGOR 7 Pro (Wavemetrics). Geometric means of kinetic parameters were determined using Excel (Microsoft) and plotted in IGOR 7 Pro. Curve fitting was performed in IGOR Pro 7 as described previously (49). To determine time constants of toxin association and dissociation (τ_{on} and τ_{off}, respectively), Peak currents during depolarizing voltage steps were plotted by time, and data were fit with a single exponential function:

$$[1] \qquad I_{Na^+} = I_{Na^+{}_0} + Ae^{-t-t_0/\tau}$$

The association rate k_{on} was determined by equation 2, or equation 3 (18) was used when the maximal block at saturating concentrations (F_{block}) was already known and k_{off} could not be determined independently:

$$[2] \qquad k_{on} = \frac{\frac{1}{\tau_{on}} - k_{off}}{[tox]},$$

$$[3] \qquad k_{on} = \frac{\frac{F_{[tox]}}{F_{block}}}{\tau_{on} * [tox]}$$

k_{off} was determined by equation 4:

$$[4] \qquad k_{off} = \frac{1}{\tau_{off}}$$

Affinity was determined kinetically as the dissociation constant K_d via equation 5:

$$[5] \qquad K_d = \frac{k_{off}}{k_{on}}$$

The slow dissociation of WT-KIIIA from WT-hNav1.7 made thorough measurement of k_{off} difficult due to limited recovery during the experiment, thus values shown here are best estimates from fits with the amplitude constrained based on the maximal current before toxin association. The resulting values of affinity are consistent with previous reporting of kinetic determination of affinity for this channel (18). Concentration-response data was collected to determine maximal block and IC_{50} was for WT-KIIIA x WT-hNav1.7 with a Hill equation 6; the Hill coefficient h was assumed to be 1 in accordance with a single binding site:

$$[6] \qquad F_{[Tox]} = \frac{F_{block}}{\left\{1 + \left(\frac{IC_{50}}{[Tox\}}^{h}\right)\right\}}$$

Maximum fractional block at saturating concentrations was determined from kinetic data and observed steady-state block ($F_{[tox]}$) for other channel and toxin variants, except where noted, according to equation 7 (18):

$$[7] \qquad F_{block} = F_{[tox]}\left(1 + \frac{K_d}{[tox]}\right)$$

The low affinity of H12A hindered precise measurement of dissociation kinetics from a lack of sufficient data points to fit during the dissociation from low percentage block, thus the rates are extrapolated from Fractional block assuming maximal block at saturating concentration of 0.877 as reported previously (18). The E919Q x D11A condition suffered from this same difficulty, thus kinetic values reported assumed similar levels of block to those observed during the E919Q x WT-KIIIA condition (0.92, Table 3). The lack of effect of the D11A variant on channel block suggests that any interactions with D11A would not reduce the level of block seen with the E919Q mutation.

Coupling coefficients (Ω) and energies ($E_{coupling}$) were calculated from the dissociation constants of the four conditions for each cycle according to equations 8 and 9, respectively (34) where "$K_d wm$" would represent the dissociation constant for WT-hNav1.7 x Toxin-variant condition:

$$[8] \qquad \Omega = \frac{K_d ww * K_d mm}{K_d wm * K_d mw}, \qquad [9] \qquad E_{coupling} = -RT \ln \Omega$$

Descriptive statistics: Arithmetic means and standard error were calculated for F_{block}, while log-scaled kinetic parameters were summarized with geometric means and standard deviations. Standard errors of kinetic parameters were obtained for the tables as the dividend of the standard deviation and the square-root of the sample size for each toxin-channel pair, as noted in parentheses in each table. Errors for coupling coefficients and coupling energies were calculated by linear propagation of error from fractional standard deviations of the reported K_d values for the toxin – channel mutant pairs used to calculate the coupling coefficients.

Figure Legends

Figure 1. **Structural model of KIIIA - hNav1.7 features eccentric binding of toxin to the outer pore**. (**A**) Structure and sequence of KIIIA (PDB: 2LXG) (17) shows alpha helical core stabilized by three disulfide bridges. (**B**) Extracellular view of our homology model of KIIIA – hNav1.7 complex based on the EeNav1.4-β1 cryo-EM structure (22). Channel domains are depicted according to color keys, and KIIIA is shown in magenta ribbon and surface. KIIIA binds eccentrically to the outer pore between DII and DIII. (**C**) Incomplete block of KIIIA revealed by side view of channel pore with KIIIA bound (magenta) and cavity volume. (**D**) Rosetta alanine scan identified residues K7, W8, R10, H12, and R14 as significant contributors to binding energy. (**E**) Heatmap of Rosetta ΔΔG on KIIIA structure shows the importance of the helical region for binding. (**F**) Interactions at KIIIA – hNav1.7 interface predicted by our model. Rosetta model of the KIIIA - hNav1.7 complex based on bacterial NavAb structure (28). (B) Extracellular view of the pore region of the KIIIA - hNav1.7 model based on eeNav1.4 structure (21) in superposition with the cryo-EM structure of the KIIIA - hNav1.2 complex Figure 1—figure supplement 1.

Figure 2. **Functional studies of toxin variants and channel mutations**. (**A**) Normalized peak I_{Na}+ from a whole cell voltage clamp experiment with 10 μM WT-KIIIA against WT-hNav1.7 resulting in incomplete block and (inset) raw current traces before toxin (black) and after toxin (blue). (**B**) Hill-fit (black) and 95% confidence interval (dashed blue) of concentration-response data for WT-KIIIA against hNav1.7 in HEK293 cells (IC_{50}=0.41±0.16 μM mean±SD, n=2-4 cells per concentration), from maximum block recorded during association experiments. Empty circles represent single cells. **(C**) Calculated Fractional block (see Materials and methods) for toxin variants and channel mutants (mean±SEM). WT x H12A block data reported by McArthur, et al.

(18) **(D**) Kinetic data from electrophysiological measurements show general agreement with Rosetta predicted energies. Alanine variants of residues K7, W8, D11, and H12 showed significant reductions in affinity (K_d)(left), little change in association (k_{on})(middle), but marked increases in toxin dissociation (k_{off})(right). Bars are geometric mean±SD from n=3-5 cells per variant (reported in Table 1), empty circles represent single cells. (**E**) Mutations to channel residues demonstrate reductions in affinity of the WT-KIIIA from Y362C, E919Q, and D923A (left), little change to toxin association (middle), and increases in dissociation (right), similar to the effects of toxin variants. Bars are geometric mean±SD from n=3-5 cells per variant (reported in table 2), empty circles represent single cells.

Figure 3. **Double mutant cycle analysis supports key pairwise interactions between KIIIA and hNav1.7**. (**A**) Thermodynamic double-mutant cycles between H12A x D923A, K7A x E919Q, and D11A x E919Q. K_d (geometric mean±SEM) listed under each channel mutant/toxin variant pair tested. Center values are coupling energies (kcal·mol^{-1}) for the interactions with errors from a linear propagation of error. (**B**) K_d, k_{on}, and k_{off} for single and double mutants. Bars are geometric mean±SD, n=2-5 cells per condition (reported in table 3), empty circles are individual cells. The double mutants for K7A x E919Q and H12A x D923A were similar to the respective single mutant conditions, while the D11A x E919Q double mutant showed a much greater reduction in affinity relative to the single mutants.

Figure 4. **Marked difference for KIIIA binding specificity among Nav channel isoforms**. (**A**) Comparisons of key residue interactions on the KIIIA - hNav1.7 model and the KIIIA - hNav1.2 structure. Domains and residue labels are depicted according to color keys. (**B**) Sequence alignment of the different Nav subtypes at the interaction site with KIIIA. Different regions are

labeled. Key interacting residues of KIIIA are labeled and colored in magenta at positions of corresponding interactions in channel residues. Superscripts show sequence number of hNav1.7.

Figure 5. **MD simulation of KIIIA - hNav1.7 and KIIIA - hNav1.2 complexes**. (**A**) Structural dynamics of KIIIA binding in hNav1.7. Snapshots of KIIIA binding configurations with hNav1.7 during the simulation, associated with the interface RMSD (left and middle panels): A1, an equilibrated binding configuration with sodium ion (orange sphere) in the selectivity filter localized at E916 and E919; A2, a relaxed configuration after the escape of selectivity filter sodium ion; A3, a binding configuration with K7, R10 reaching toward the P2-helix in DIV. Heatmap showing fractional contacts between key residues on KIIIA and hNav1.7 channel during the simulation (right panel). (**B**) Structural dynamics of KIIIA binding in hNav1.2. Snapshots of KIIIA binding configurations with hNav1.2 during the simulation, associated with the interface RMSD (left and middle panels): B1, an equilibrated configuration with sodium ion (orange sphere) in the selectivity filter localized at E942 and E945; B2, a binding configuration with stable interaction of R10 with D1426 and K7 with E945. Heatmap showing fractional contacts between key residues on KIIIA and hNav1.2 channel during the simulation (right panel). (C) Time series of representative atomic contacts of K7 and R10 interactions with the hNav1.7 (left panel) and hNav1.2 (right panel) residues in the simulations. Labels show residue numbers and their associated atom names (in parenthesis).

Figure 1—figure supplement 1. **Rosetta models of hNav1.7 – KIIIA complex. Domains are depicted according to color keys**. (**A**) Extracellular view of the pore region of the Rosetta model of the KIIIA - hNav1.7 complex based on bacterial NavAb structure (28). (**B**) Extracellular view

of the pore region of the KIIIA - hNav1.7 model based on eeNav1.4 structure (22) in superposition with the cryo-EM structure of the KIIIA - hNav1.2 complex (21).

Figure 2—figure supplement 1. **Representative data from functional studies of toxin variants and channel mutations**. (**A**) Normalized peak I_{Na}+ from a whole cell voltage clamp experiments with WT-hNav1.7 in the presence of toxin variants as stated in each plot, exponential fits of association and dissociation shown in blue. Raw current traces (inset) before toxin (black) and after toxin addition (blue). (**B**) Normalized peak I_{Na}+ from whole cell voltage clamp experiments with hNav1.7 mutants as labeled in the presence of WT-KIIIA as in panel A.

Figure 3—figure supplement 1. Representative data from double-mutant cycle analysis. (**A**) Normalized peak I_{Na}+ from a whole cell voltage clamp experiments with WT x WT, single, and double mutations D923A and H12A as indicated by column and row labels. Exponential fits of association and dissociation shown in blue. Raw current traces (inset) before toxin (black) and after toxin addition (blue). (**B**) Normalized peak I_{Na}+ from a whole cell voltage clamp experiments, as in panel A for the two residue pairs E919 x K7 and E919 x D11.

Figure 4—figure supplement 1. **Differences in interactions of KIIIA residues D11 (left panel) and R10 (right panel) between the KIIIA - hNav1.7 model and the KIIIA - hNav1.2 structure**. Domains and labels are depicted according to color keys. Both alternative sidechain rotamers of KIIIA R10 residue identified in the KIIIA - hNav1.2 structure are shown.

Figure 5—figure supplement 1. **Binding of KIIIA to hNav1.7 and hNav1.2 in A3 configuration (hNav1.7) and B2 configuration (hNav1.2)**. (**A**) Extracellular view suggests more complete block of KIIIA in A3 configuration on hNav1.7 than in B2 configuration on hNav1.2. Domains are depicted according to color keys and key interacting channel residues on the P2-helix are labeled. (**B**) Tunnel search with CAVER in the hNav1.7 – KIIIA binding configuration A3. A

single passage connecting the selectivity filter and the open space between the P1-helix in DIII and the P2-helix in DIV, was identified and located under KIIIA and disconnected from the bulk region. K7 and R10 residues on KIIIA shown in stick representation appear to prevent connection to the bulk region. (**C**) Multiple passages were detected in a tunnel search with CAVER in the KIIIA - hNav1.2 binding configuration B2 spanning from selectivity filter through the side of KIIIA to the bulk region.

Figure 5—figure supplement 2. **MD simulation of KIIIA - hNav1.7 model**. (**A**) Time series of representative atomic contacts of W8, D11, H12, and R14 interactions with the hNav1.7 residues. Labels show residue numbers and their associated atom names (in parenthesis). (**B**) A snapshot of the last frame of the 1μs simulation. Domains are depicted according to color keys and channel residues that have high fractional contacts in Figure 5A are shown in stick representation and labeled.

Figure 5—figure supplement 3. **MD simulation of KIIIA - hNav1.2 model**. (**A**) Time series of representative atomic contacts of W8, D11, H12, and R14 interactions with the hNav1.2 residues. Labels show residue numbers and their associated atom names (in parenthesis). (**B**) A snapshot of the last frame of the 1μs simulation. Domains are depicted according to color keys and channel residues that have high fractional contacts in Figure 5B are shown in stick representation and labeled.

Video 1. MD simulation of KIIIA - hNav1.7 complex highlighting dynamics of K7 and R10 interactions with E364 (DI) and D1690 (DIV).

Video 2. MD simulation of KIIIA - hNav1.2 complex highlighting dynamics of K7 and R10 interactions with E945 (DII) and D1426 (DIII).

References

1. Hille B (2001) *Ion Channels of Excitable Membranes* (Sinauer Associates, Sunderland, MA)) 3rd Ed.
2. Catterall WA (2014) Structure and function of voltage-gated sodium channels at atomic resolution. *Exp Physiol* 99(1):35-51.
3. Ahern CA, Payandeh J, Bosmans F, & Chanda B (2016) The hitchhiker's guide to the voltage-gated sodium channel galaxy. *J Gen Physiol* 147(1):1-24.
4. Catterall WA, Goldin AL, & Waxman SG (2005) International Union of Pharmacology. XLVII. Nomenclature and structure-function relationships of voltage-gated sodium channels. *Pharmacol Rev* 57(4):397-409.
5. Dib-Hajj SD & Waxman SG (2019) Sodium Channels in Human Pain Disorders: Genetics and Pharmacogenomics. *Annu Rev Neurosci*.
6. Bennett DL, Clark AJ, Huang J, Waxman SG, & Dib-Hajj SD (2019) The Role of Voltage-Gated Sodium Channels in Pain Signaling. *Physiol Rev* 99(2):1079-1151.
7. Dib-Hajj SD, Yang Y, Black JA, & Waxman SG (2013) The Na(V)1.7 sodium channel: from molecule to man. *Nat Rev Neurosci* 14(1):49-62.
8. Nguyen PT, DeMarco KR, Vorobyov I, Clancy CE, & Yarov-Yarovoy V (2019) Structural basis for antiarrhythmic drug interactions with the human cardiac sodium channel. *Proc Natl Acad Sci U S A* 116(8):2945-2954.
9. Yarov-Yarovoy V, *et al.* (2002) Role of amino acid residues in transmembrane segments IS6 and IIS6 of the Na+ channel alpha subunit in voltage-dependent gating and drug block. *J Biol Chem* 277(38):35393-35401.

10. Yarov-Yarovoy V, *et al.* (2001) Molecular determinants of voltage-dependent gating and binding of pore-blocking drugs in transmembrane segment IIIS6 of the Na(+) channel alpha subunit. *J Biol Chem* 276(1):20-27.

11. Ragsdale DS, McPhee JC, Scheuer T, & Catterall WA (1994) Molecular determinants of state-dependent block of Na+ channels by local anesthetics. *Science* 265(5179):1724-1728.

12. Payandeh J & Hackos DH (2018) Selective Ligands and Drug Discovery Targeting the Voltage-Gated Sodium Channel Nav1.7. *Handb Exp Pharmacol* 246:271-306.

13. Wilson MJ, *et al.* (2011) mu-Conotoxins that differentially block sodium channels NaV1.1 through 1.8 identify those responsible for action potentials in sciatic nerve. *Proc Natl Acad Sci U S A* 108(25):10302-10307.

14. Gilchrist J, Olivera BM, & Bosmans F (2014) Animal toxins influence voltage-gated sodium channel function. *Handb Exp Pharmacol* 221:203-229.

15. French RJ, Yoshikami D, Sheets MF, & Olivera BM (2010) The tetrodotoxin receptor of voltage-gated sodium channels--perspectives from interactions with micro-conotoxins. *Mar Drugs* 8(7):2153-2161.

16. Zhang MM, *et al.* (2007) Structure/function characterization of micro-conotoxin KIIIA, an analgesic, nearly irreversible blocker of mammalian neuronal sodium channels. *J Biol Chem* 282(42):30699-30706.

17. Khoo KK, *et al.* (2012) Distinct disulfide isomers of mu-conotoxins KIIIA and KIIIB block voltage-gated sodium channels. *Biochemistry* 51(49):9826-9835.

18. McArthur JR, *et al.* (2011) Interactions of key charged residues contributing to selective block of neuronal sodium channels by mu-conotoxin KIIIA. *Mol Pharmacol* 80(4):573-584.

19. Zhang MM, *et al.* (2009) Synergistic and antagonistic interactions between tetrodotoxin and mu-conotoxin in blocking voltage-gated sodium channels. *Channels (Austin)* 3(1):32-38.

20. Korkosh VS, Zhorov BS, & Tikhonov DB (2014) Folding similarity of the outer pore region in prokaryotic and eukaryotic sodium channels revealed by docking of conotoxins GIIIA, PIIIA, and KIIIA in a NavAb-based model of Nav1.4. *J Gen Physiol* 144(3):231-244.

21. Pan X, *et al.* (2019) Molecular basis for pore blockade of human Na(+) channel Nav1.2 by the mu-conotoxin KIIIA. *Science* 363(6433):1309-1313.

22. Yan Z, *et al.* (2017) Structure of the Nav1.4-beta1 Complex from Electric Eel. *Cell* 170(3):470-482 e411.

23. Song Y, *et al.* (2013) High-resolution comparative modeling with RosettaCM. *Structure* 21(10):1735-1742.

24. Bender BJ, *et al.* (2016) Protocols for Molecular Modeling with Rosetta3 and RosettaScripts. *Biochemistry* 55(34):4748-4763.

25. Gray JJ, *et al.* (2003) Protein-protein docking with simultaneous optimization of rigid-body displacement and side-chain conformations. *J Mol Biol* 331(1):281-299.

26. Wang C, Bradley P, & Baker D (2007) Protein-protein docking with backbone flexibility. *J Mol Biol* 373(2):503-519.

27. Kimball IH, Nguyen PT, Sack JT, & Yarov-Yarovoy V (2016) Mapping the Nav1.7 Channel Interaction with the Conotoxin KIIIA. *Biophysical Journal* 110(3):437a-437a.

28. Payandeh J, Scheuer T, Zheng N, & Catterall WA (2011) The crystal structure of a voltage-gated sodium channel. *Nature* 475(7356):353-358.

29. Kubota T, *et al.* (2017) Mapping of voltage sensor positions in resting and inactivated mammalian sodium channels by LRET. *Proc Natl Acad Sci U S A* 114(10):E1857-E1865.

30. Shen H, Liu D, Wu K, Lei J, & Yan N (2019) Structures of human Nav1.7 channel in complex with auxiliary subunits and animal toxins. *Science* 363(6433):1303-1308.

31. Shen H, *et al.* (2018) Structural basis for the modulation of voltage-gated sodium channels by animal toxins. *Science* 362(6412):eaau2596.

32. Kimball IH, Nguyen PT, Sack JT, & Yarov-Yarovoy V (2018) Assessing the Structural Basis of mu-Conotoxin KIIIA Inhibition of the Voltage-Gated Sodium Channel Nav1.7. *Biophysical Journal* 114(3):635a-635a.

33. Penzotti JL, Fozzard HA, Lipkind GM, & Dudley SC, Jr. (1998) Differences in saxitoxin and tetrodotoxin binding revealed by mutagenesis of the Na+ channel outer vestibule. *Biophys J* 75(6):2647-2657.

34. Hidalgo P & MacKinnon R (1995) Revealing the architecture of a K+ channel pore through mutant cycles with a peptide inhibitor. *Science* 268(5208):307-310.

35. Ranganathan R, Lewis JH, & MacKinnon R (1996) Spatial localization of the K+ channel selectivity filter by mutant cycle-based structure analysis. *Neuron* 16(1):131-139.

36. Schreiber G & Fersht AR (1995) Energetics of protein-protein interactions: Analysis ofthe Barnase-Barstar interface by single mutations and double mutant cycles. *Journal of Molecular Biology* 248(2):478-486.

37. Pan X, *et al.* (2018) Structure of the human voltage-gated sodium channel Nav1.4 in complex with beta1. *Science* 362(6412):eaau2486.

38. Shaw DE, *et al.* (2014) Anton 2: Raising the bar for performance and programmability in a special-purpose molecular dynamics supercomputer. *Sc14: International Conference for High Performance Computing, Networking, Storage and Analysis*:41-53.

39. Wang RY, *et al.* (2016) Automated structure refinement of macromolecular assemblies from cryo-EM maps using Rosetta. *Elife* 5:e17219.

40. Bonneau R, *et al.* (2002) De novo prediction of three-dimensional structures for major protein families. *J Mol Biol* 322(1):65-78.

41. Fleishman SJ, *et al.* (2011) RosettaScripts: a scripting language interface to the Rosetta macromolecular modeling suite. *PloS one* 6(6):e20161.

42. Jo S, Kim T, Iyer VG, & Im W (2008) CHARMM-GUI: a web-based graphical user interface for CHARMM. *J Comput Chem* 29(11):1859-1865.

43. Jiang W, *et al.* (2011) High-performance scalable molecular dynamics simulations of a polarizable force field based on classical Drude oscillators in NAMD. *J Phys Chem Lett* 2(2):87-92.

44. Gasteiger E, *et al.* (2005) Protein Identification and Analysis Tools on the ExPASy Server;. *The Proteomics Protocols Handbook*, ed Walker JM (Humana Press), pp 571-607.

45. Pettersen EF, *et al.* (2004) UCSF Chimera--a visualization system for exploratory research and analysis. *J Comput Chem* 25(13):1605-1612.

46. Humphrey W, Dalke A, & Schulten K (1996) VMD: visual molecular dynamics. *J Mol Graph* 14(1):33-38, 27-38.

47. Hadley W (2016) *Ggplot2* (Springer Science+Business Media, LLC, New York, NY) p pages cm.

48. Chovancova E, *et al.* (2012) CAVER 3.0: a tool for the analysis of transport pathways in dynamic protein structures. *PLoS Comput Biol* 8(10):e1002708.

49. Dockendorff C, *et al.* (2018) Synthetic Analogues of the Snail Toxin 6-Bromo-2-mercaptotryptamine Dimer (BrMT) Reveal That Lipid Bilayer Perturbation Does Not Underlie Its Modulation of Voltage-Gated Potassium Channels. *Biochemistry* 57(18):2733-2743.

Figure 1

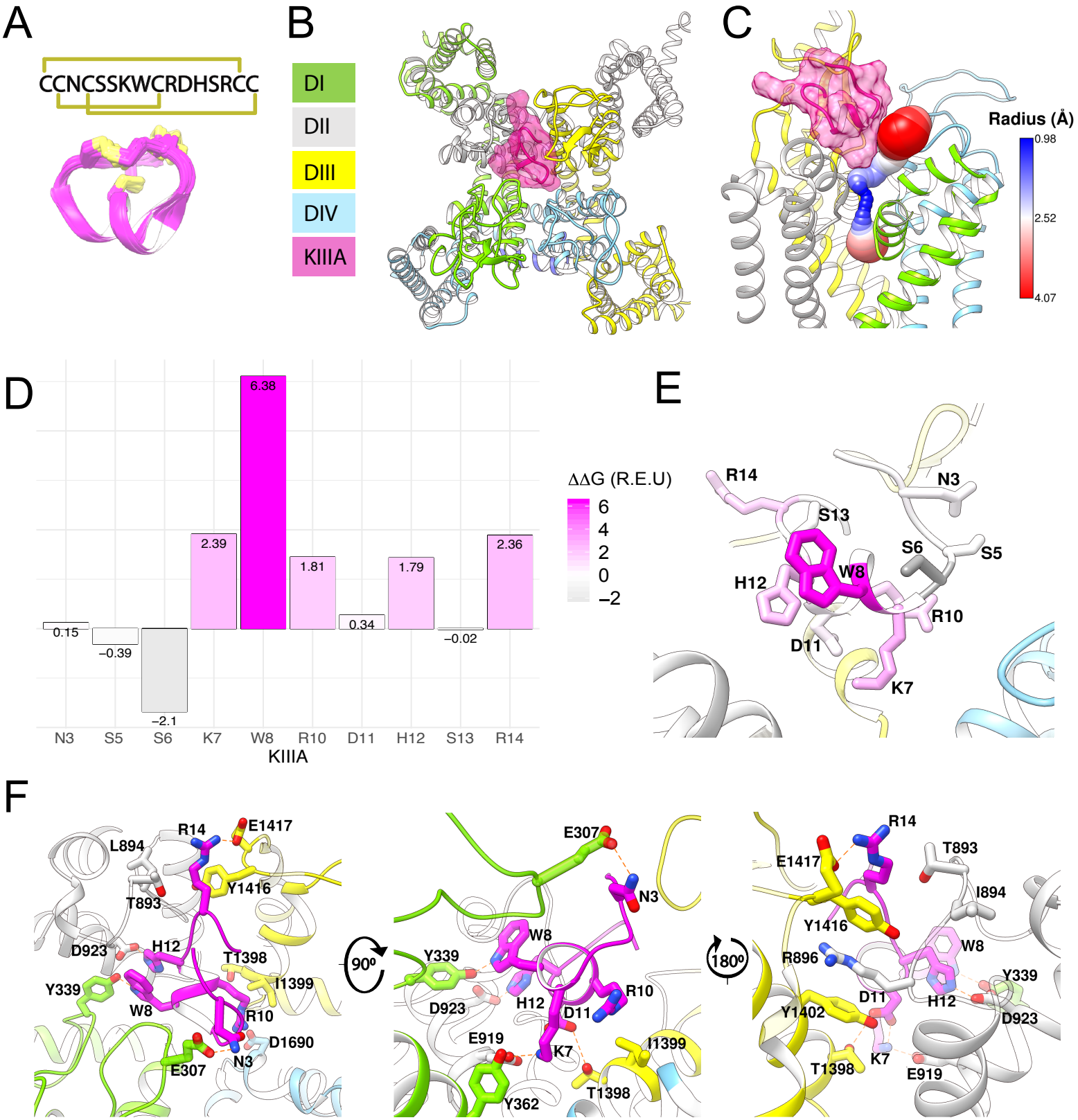
A
CCNCSSKWCRDHSRCC
B
DI
DII
DIII
DIV
KIIIA
C
Radius (Å)
0.98
2.52
4.07
D
6.38
2.39
1.81
1.79
2.36
0.15
−0.39
−2.1
0.34
−0.02
N3
S5
S6
K7
W8
R10
D11
H12
S13
R14
KIIIA
ΔΔG (R.E.U)
6
4
2
0
−2
E
R14
N3
S13
S6
S5
H12
W8
R10
D11
K7
F
R14
E1417
L894
T893
Y1416
D923
H12
T1398
I1399
Y339
W8
R10
D1690
E307
N3
90º
E307
N3
W8
Y339
R10
D923
H12
D11
E919
K7
I1399
Y362
T1398
180º
R14
T893
E1417
I894
Y1416
W8
R896
Y339
D11
H12
Y1402
D923
T1398
K7
E919

Figure 2

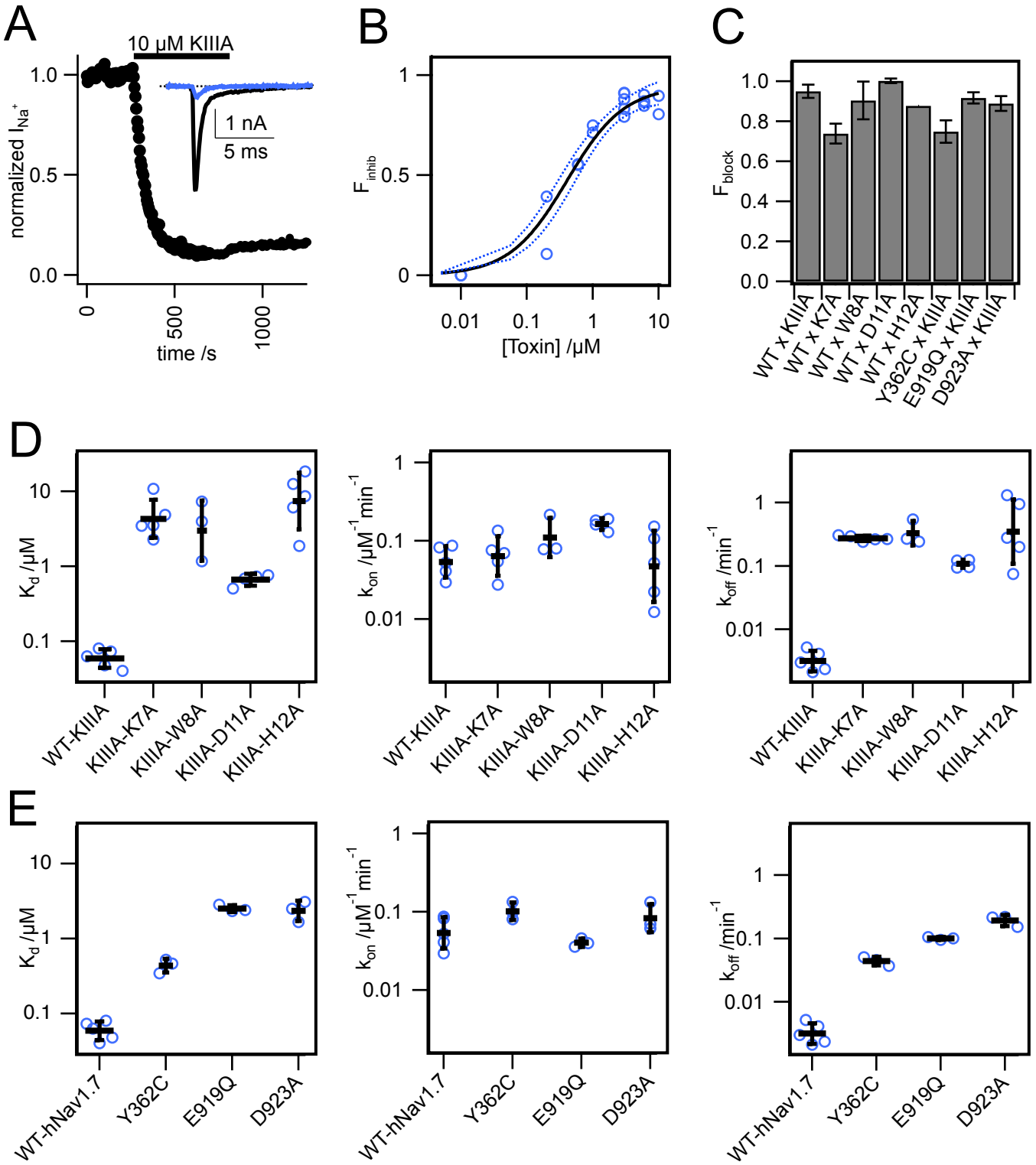
A
10 μM KIIIA
1 nA
5 ms
normalized I_{Na^+}
time /s
B
F_{inhib}
[Toxin] /μM
C
F_{block}
WT x KIIIA
WT x K7A
WT x W8A
WT x D11A
WT x H12A
Y362C x KIIIA
E919Q x KIIIA
D923A x KIIIA
D
K_d /μM
k_{on} /μM^{-1}min^{-1}
k_{off} /min^{-1}
WT-KIIIA
KIIIA-K7A
KIIIA-W8A
KIIIA-D11A
KIIIA-H12A
E
WT-hNav1.7
Y362C
E919Q
D923A

Figure 3

A

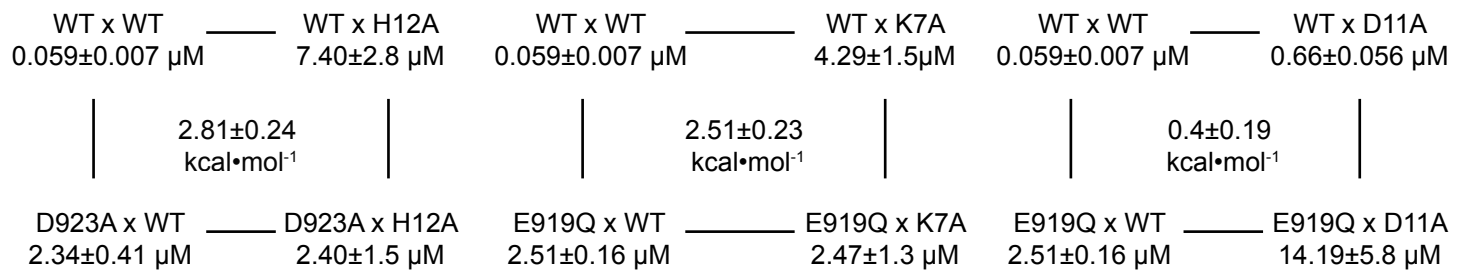

B

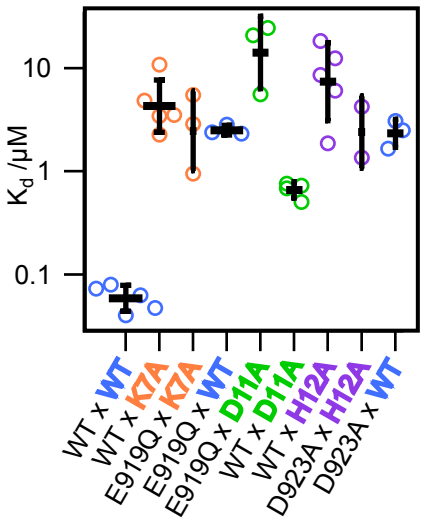

C

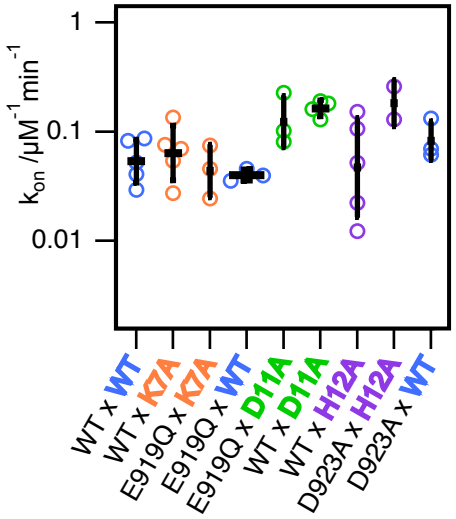

D

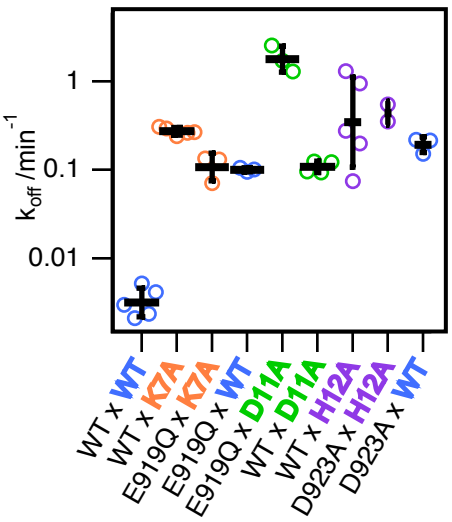

Figure 4

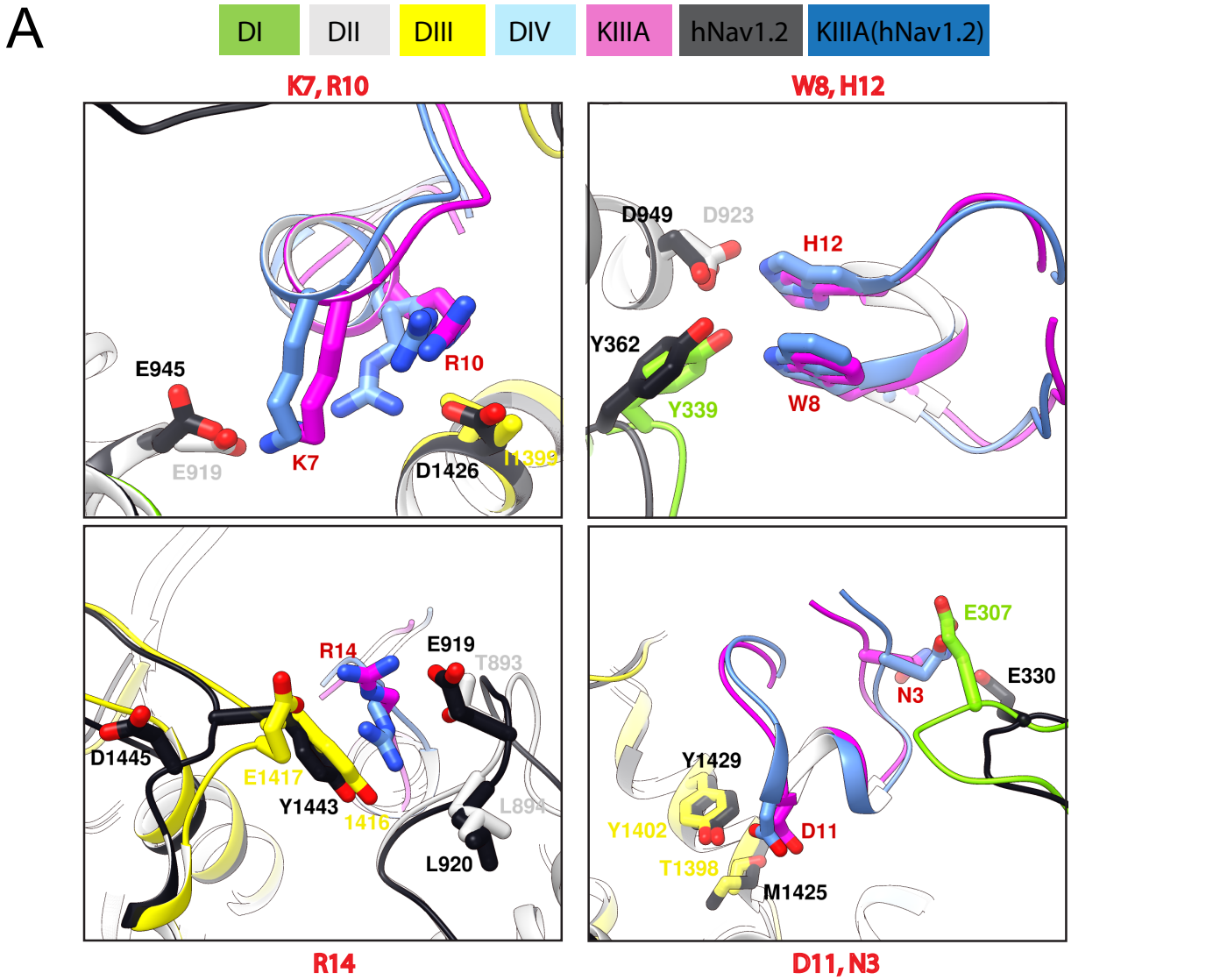
A
DI
DII
DIII
DIV
KIIIA
hNav1.2
KIIIA(hNav1.2)
K7, R10
E945
E919
K7
R10
D1426
T1398
W8, H12
D949
D923
H12
Y362
Y339
W8
R14
E919
T893
D1445
E1417
Y1443
1416
L894
L920
E307
E330
N3
Y1429
Y1402
D11
T1398
M1425
R14
D11, N3

B

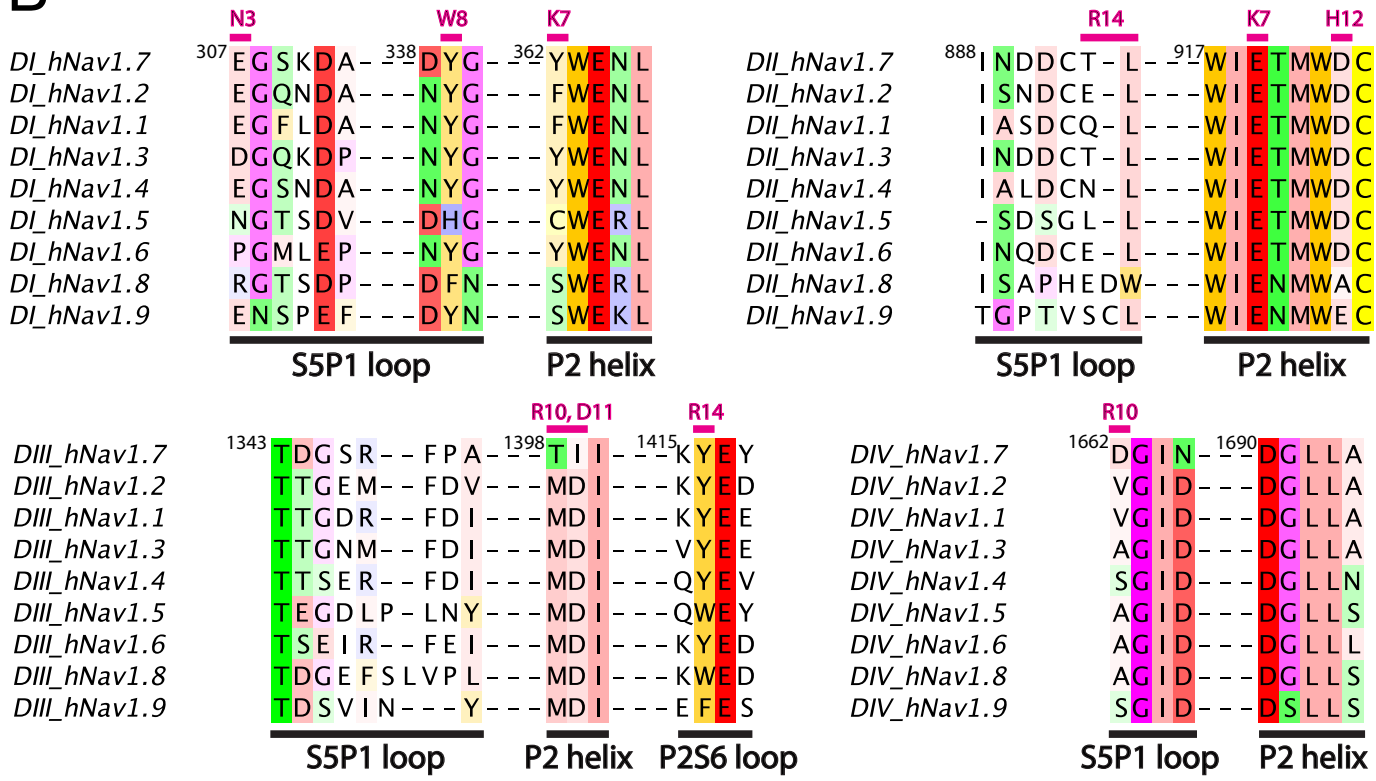
N3
W8
K7
DI_hNav1.7 307 EGSKDA---338DYG---362YWENL
DI_hNav1.2 EGQNDA---NYG---FWENL
DI_hNav1.1 EGFLDA---NYG---FWENL
DI_hNav1.3 DGQKDP---NYG---YWENL
DI_hNav1.4 EGSNDA---NYG---YWENL
DI_hNav1.5 NGTSDV---DHG---CWERL
DI_hNav1.6 PGMLEP---NYG---YWENL
DI_hNav1.8 RGTSDP---DFN---SWERL
DI_hNav1.9 ENSPEF---DYN---SWEKL
S5P1 loop
P2 helix
R14
K7
H12
DII_hNav1.7 888 INDDCT-L---917WIETMWDC
DII_hNav1.2 ISNDCE-L---WIETMWDC
DII_hNav1.1 IASDCQ-L---WIETMWDC
DII_hNav1.3 INDDCT-L---WIETMWDC
DII_hNav1.4 IALDCN-L---WIETMWDC
DII_hNav1.5 -SDSGL-L---WIETMWDC
DII_hNav1.6 INQDCE-L---WIETMWDC
DII_hNav1.8 ISAPHEDW---WIENMWAC
DII_hNav1.9 TGPTVSCL---WIENMWEC
S5P1 loop
P2 helix
R10, D11
R14
DIII_hNav1.7 1343 TDGSR--FPA---1398TII---1415KYEY
DIII_hNav1.2 TTGEM--FDV---MDI---KYED
DIII_hNav1.1 TTGDR--FDI---MDI---KYEE
DIII_hNav1.3 TTGNM--FDI---MDI---VYEE
DIII_hNav1.4 TTSER--FDI---MDI---QYEV
DIII_hNav1.5 TEGDLP-LNY---MDI---QWEY
DIII_hNav1.6 TSEIR--FEI---MDI---KYED
DIII_hNav1.8 TDGEFSLVPL---MDI---KWED
DIII_hNav1.9 TDSVIN---Y---MDI---EFES
S5P1 loop
P2 helix
P2S6 loop
R10
DIV_hNav1.7 1662 DGIN---1690DGLLA
DIV_hNav1.2 VGID---DGLLA
DIV_hNav1.1 VGID---DGLLA
DIV_hNav1.3 AGID---DGLLA
DIV_hNav1.4 SGID---DGLLN
DIV_hNav1.5 AGID---DGLLS
DIV_hNav1.6 AGID---DGLLL
DIV_hNav1.8 AGID---DGLLS
DIV_hNav1.9 SGID---DSLLS
S5P1 loop
P2 helix

Figure 5

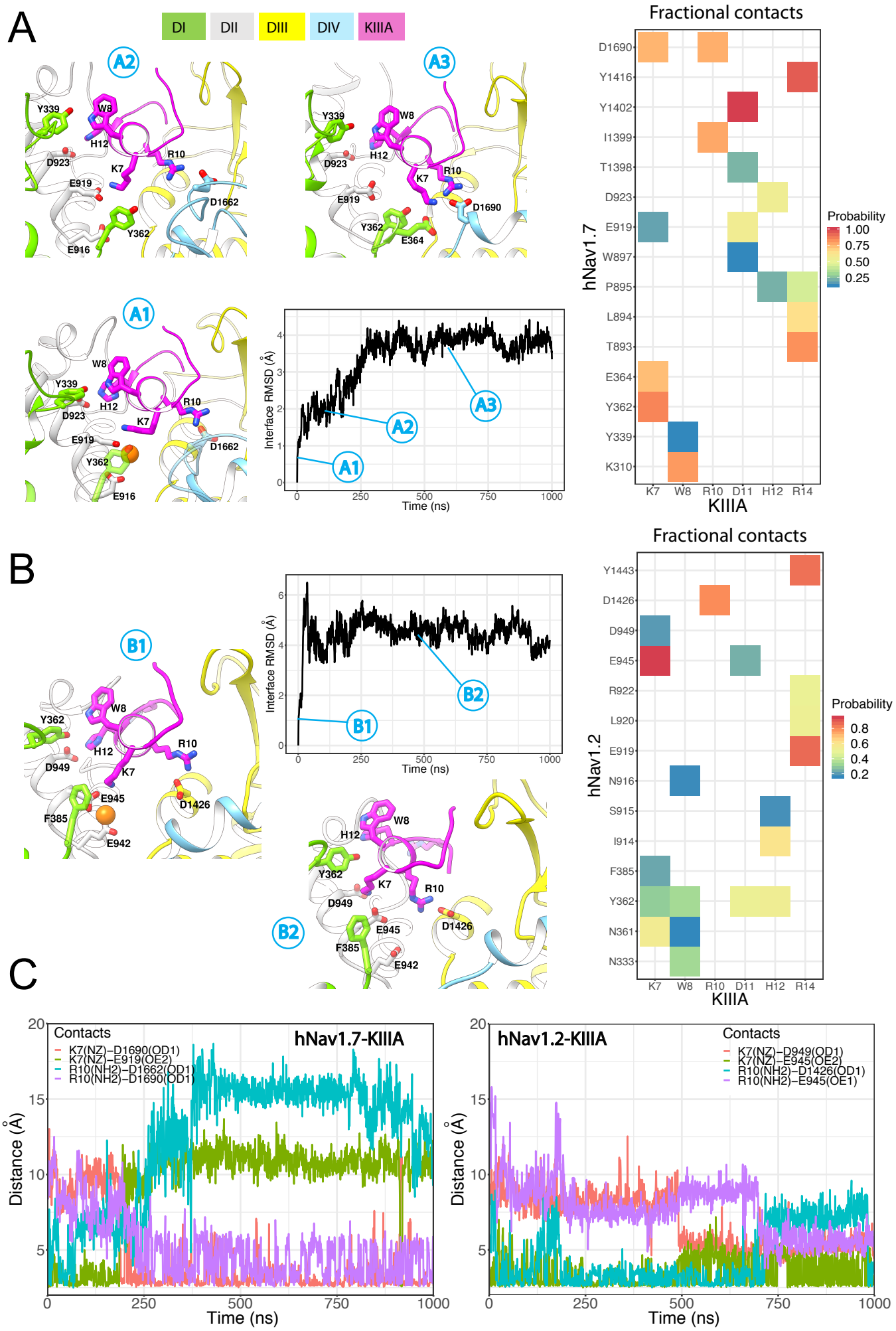
A
DI
DII
DIII
DIV
KIIIA
A1
A2
A3
Y339
W8
H12
R10
D923
K7
E919
D1662
Y362
E916
D1690
E364
Interface RMSD (Å)
Time (ns)
Fractional contacts
hNav1.7
KIIIA
K7
W8
R10
D11
H12
R14
D1690
Y1416
Y1402
I1399
T1398
D923
E919
W897
P895
L894
T893
E364
Y362
Y339
K310
Probability
1.00
0.75
0.50
0.25
B
B1
B2
Y362
W8
H12
R10
D949
K7
E945
D1426
F385
E942
Interface RMSD (Å)
Time (ns)
Fractional contacts
hNav1.2
KIIIA
Y1443
D1426
D949
E945
R922
L920
E919
N916
S915
I914
F385
Y362
N361
N333
Probability
0.8
0.6
0.4
0.2
C
hNav1.7-KIIIA
Contacts
K7(NZ)–D1690(OD1)
K7(NZ)–E919(OE2)
R10(NH2)–D1662(OD1)
R10(NH2)–D1690(OD1)
Distance (Å)
Time (ns)
hNav1.2-KIIIA
Contacts
K7(NZ)–D949(OD1)
K7(NZ)–E945(OE2)
R10(NH2)–D1426(OD1)
R10(NH2)–E945(OE1)
Distance (Å)
Time (ns)

Figure 1—figure supplement 1

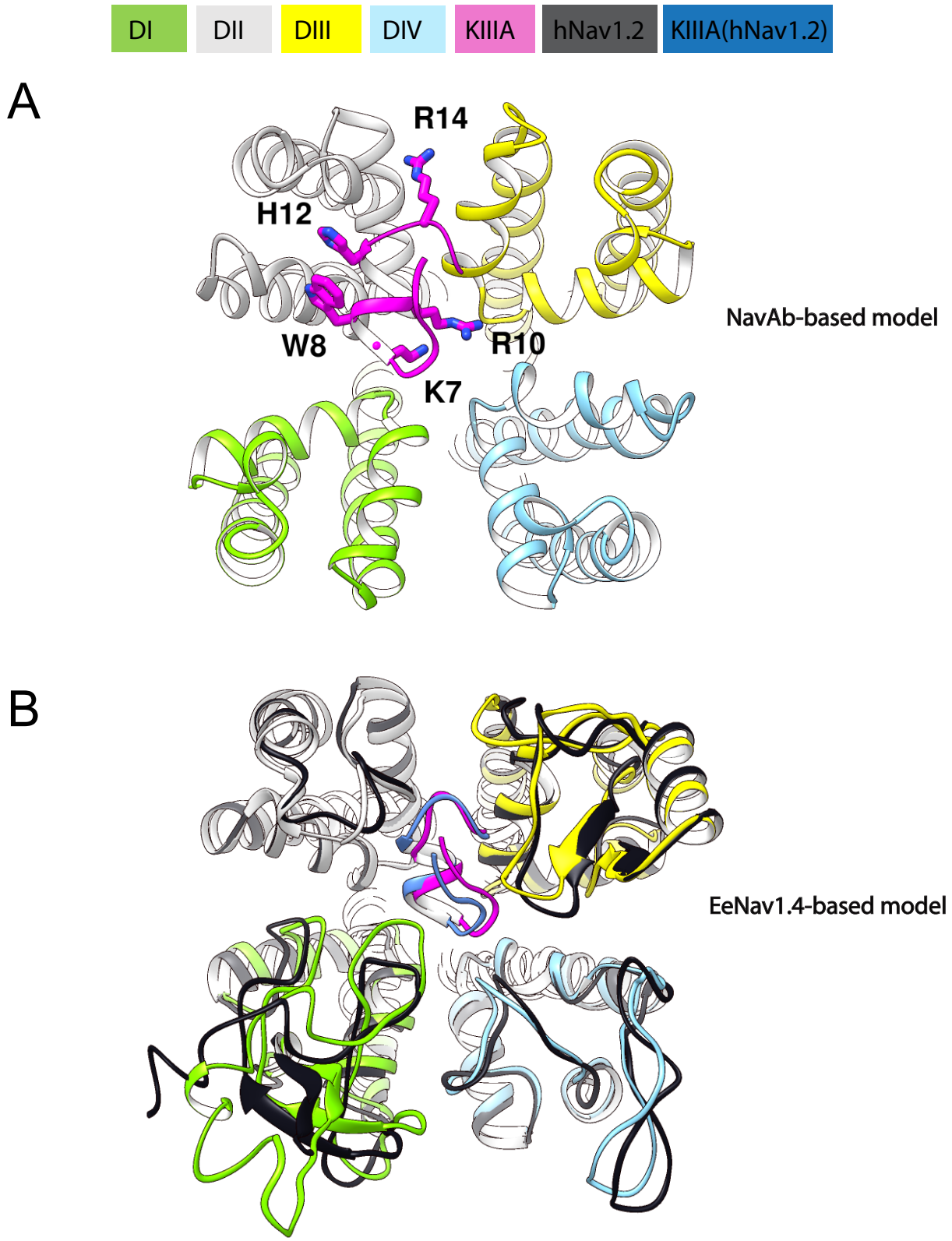

Figure 2—figure supplement 1

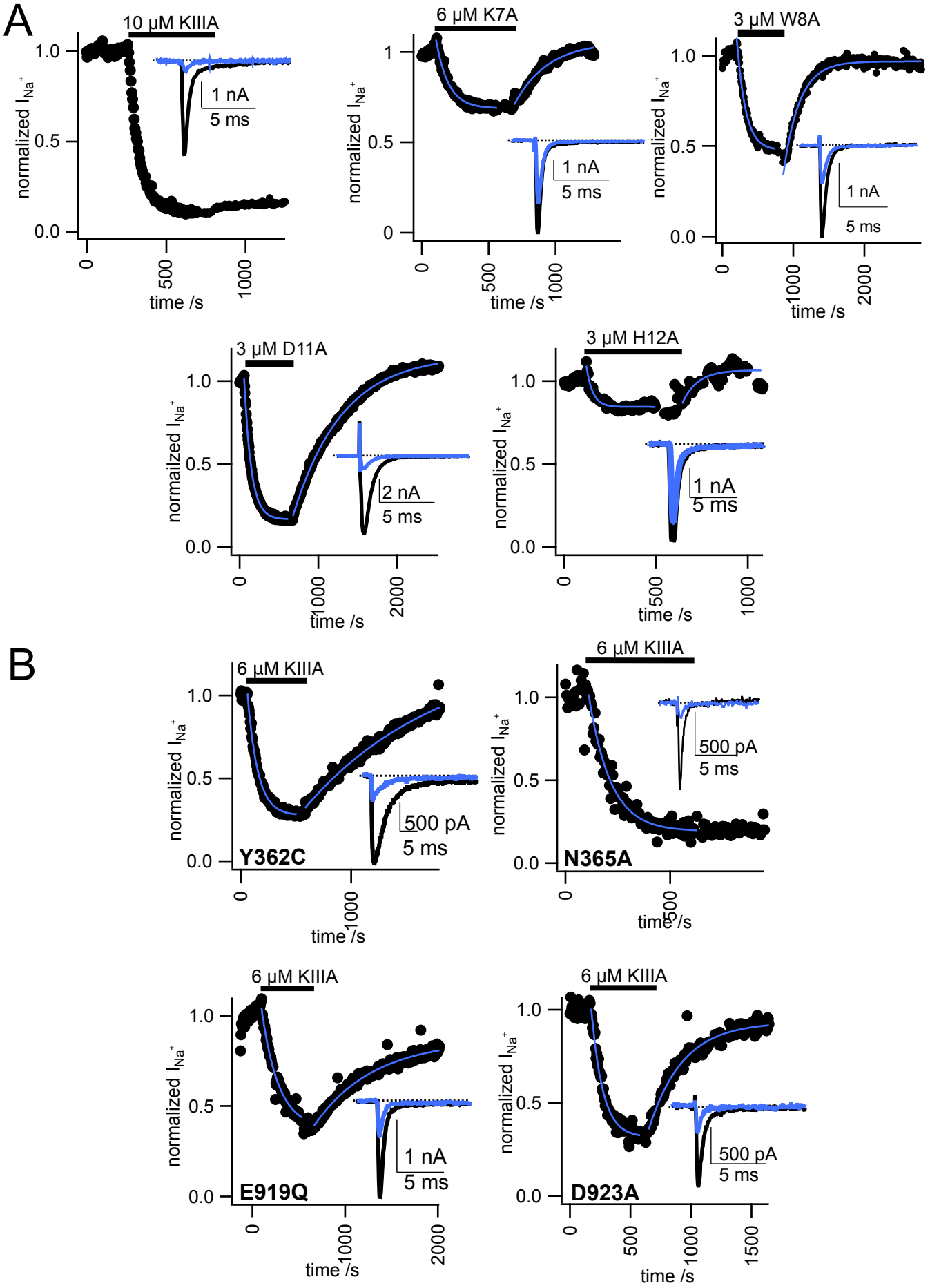

Figure 3—figure supplement 1

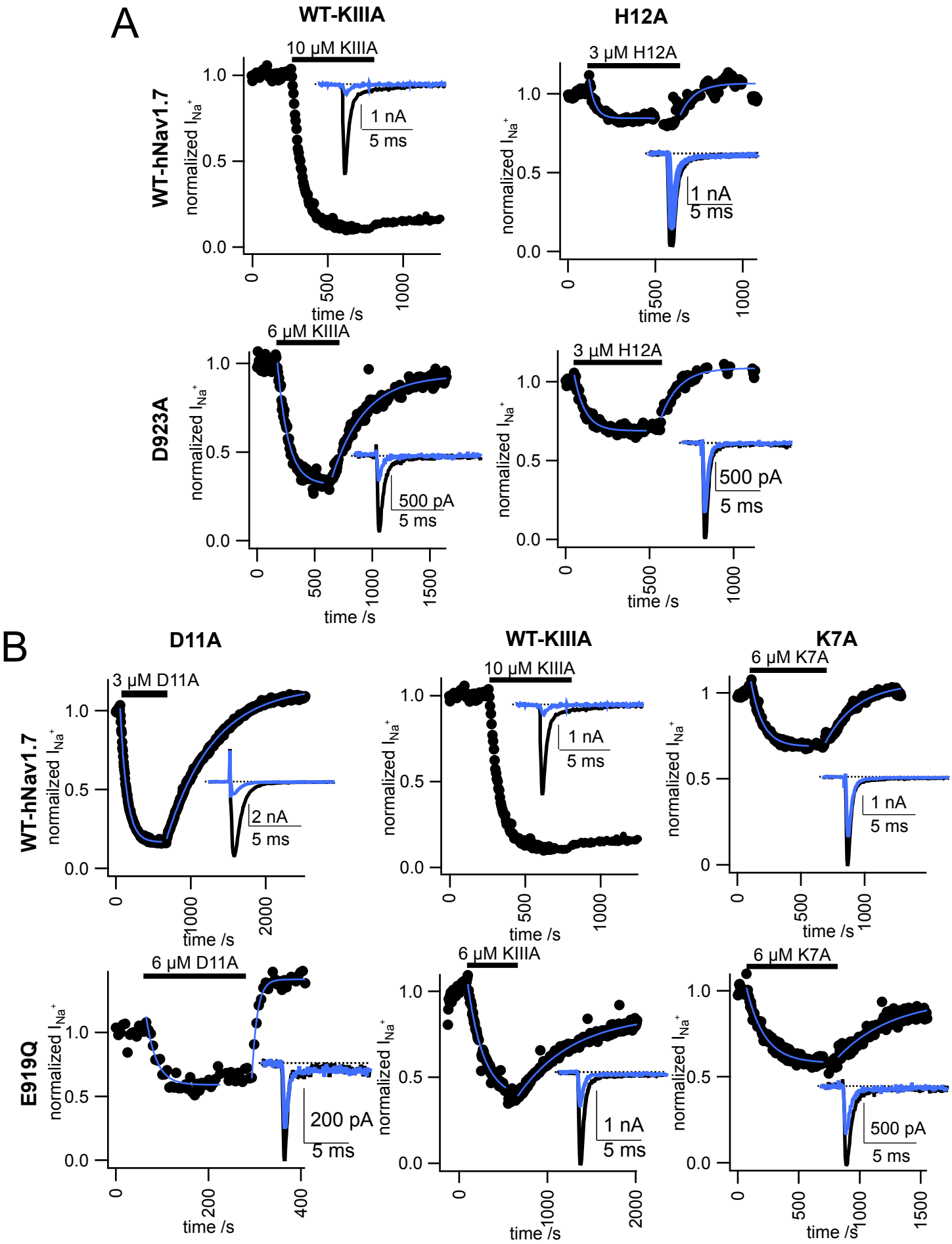

Figure 4—figure supplement 1

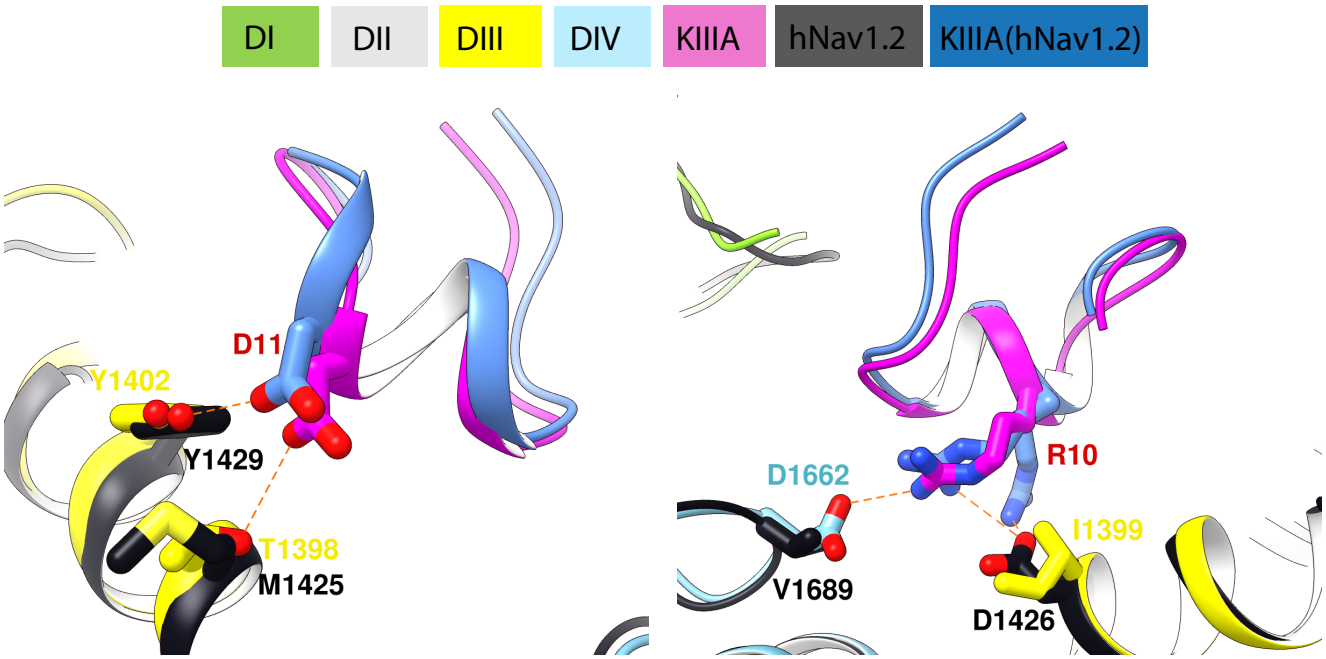

Figure 5—figure supplement 1

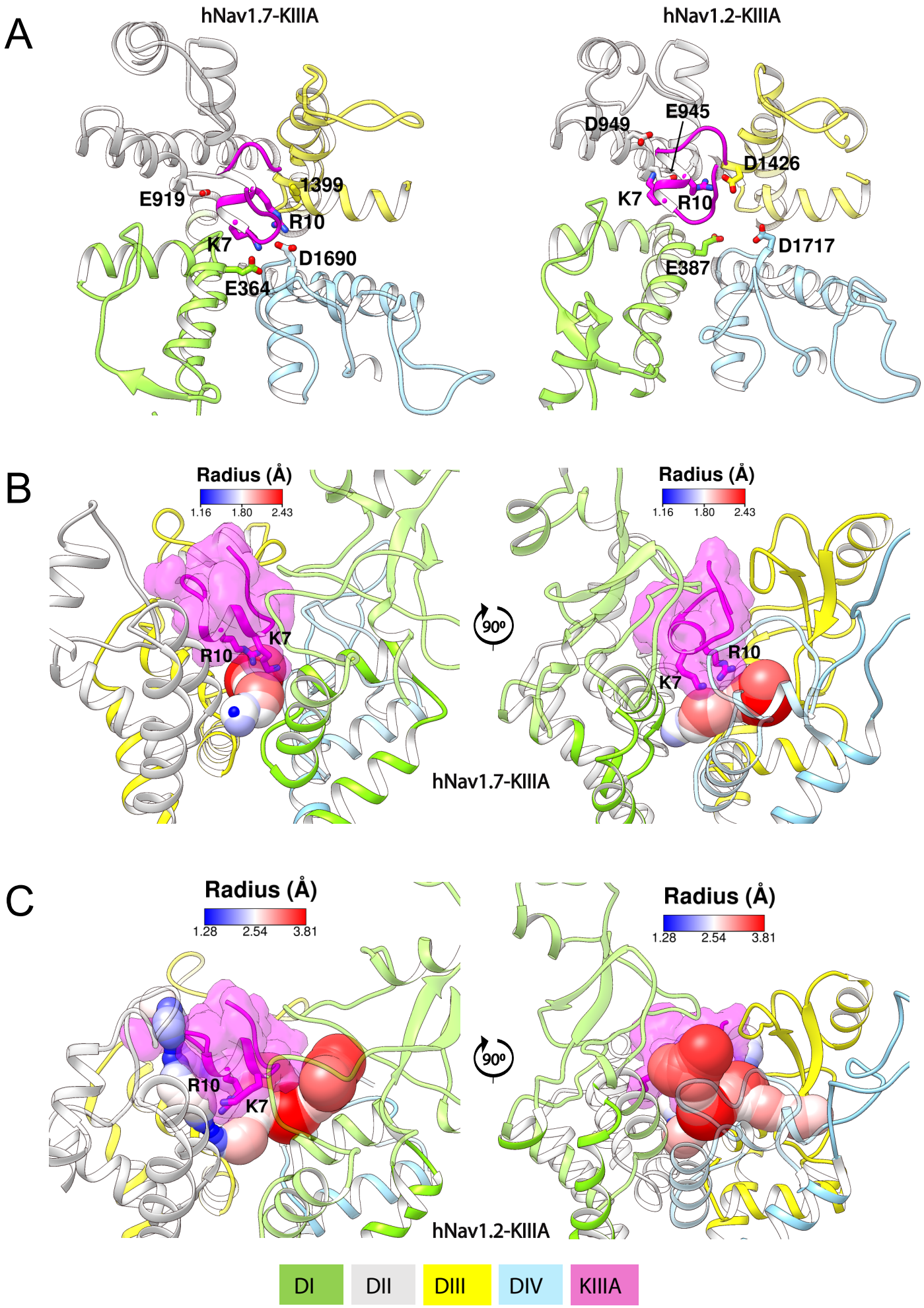

Figure 5—figure supplement 2

A

Representative hNav1.7-KIIIA atomic contacts

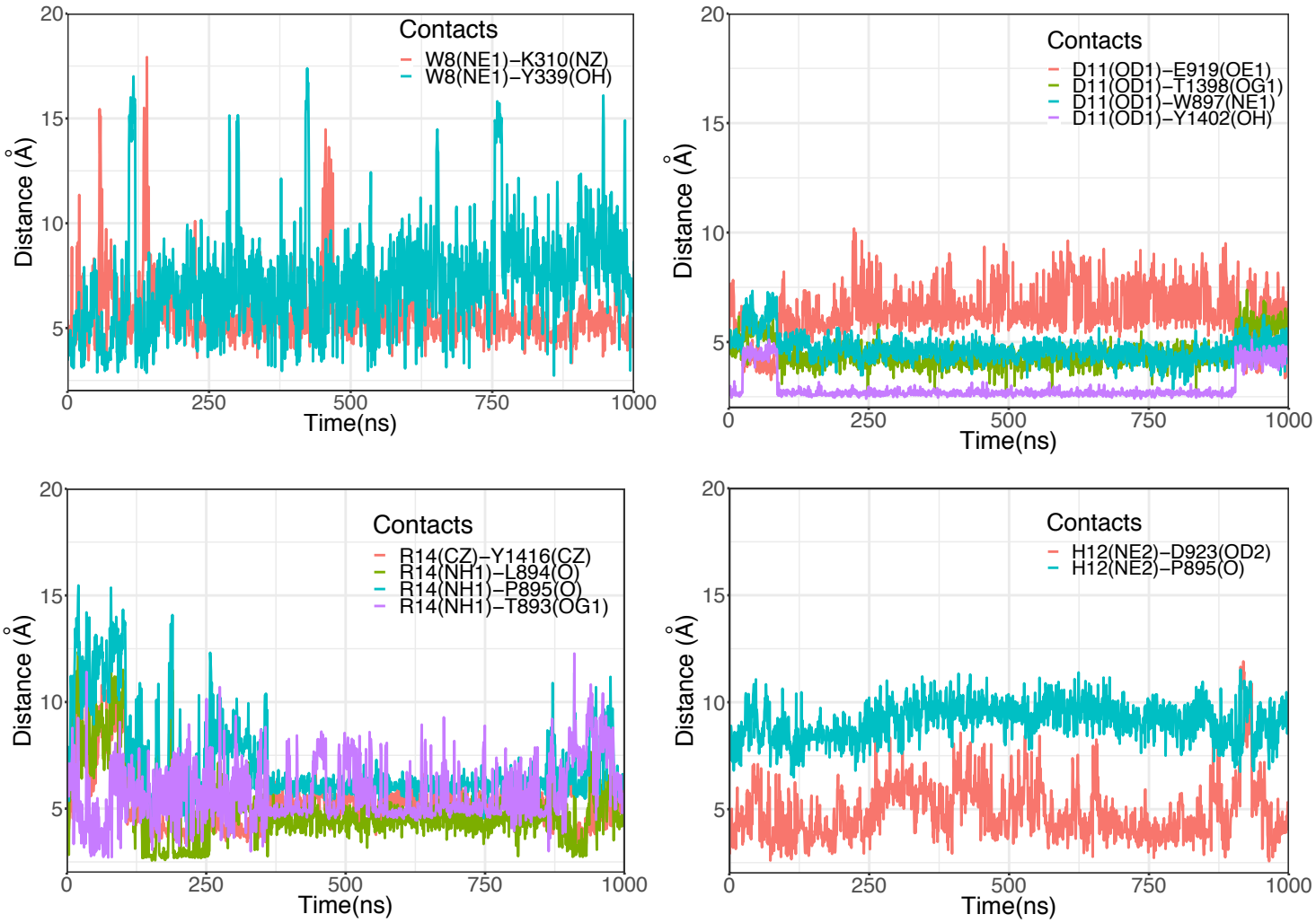

B

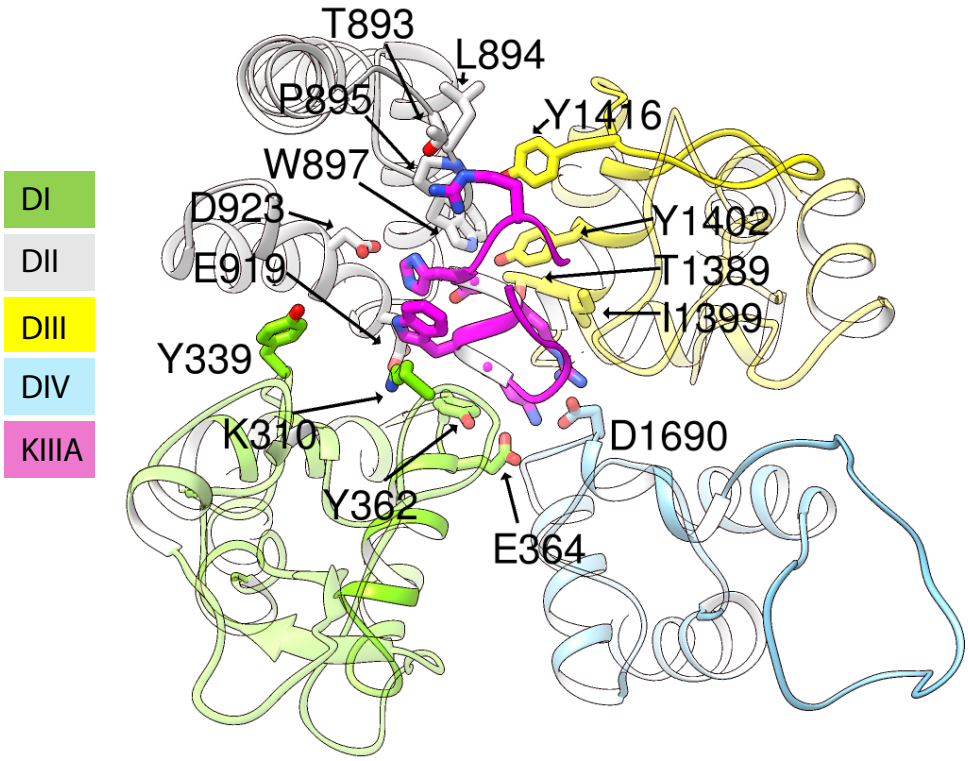

Figure 5—figure supplement 3

A

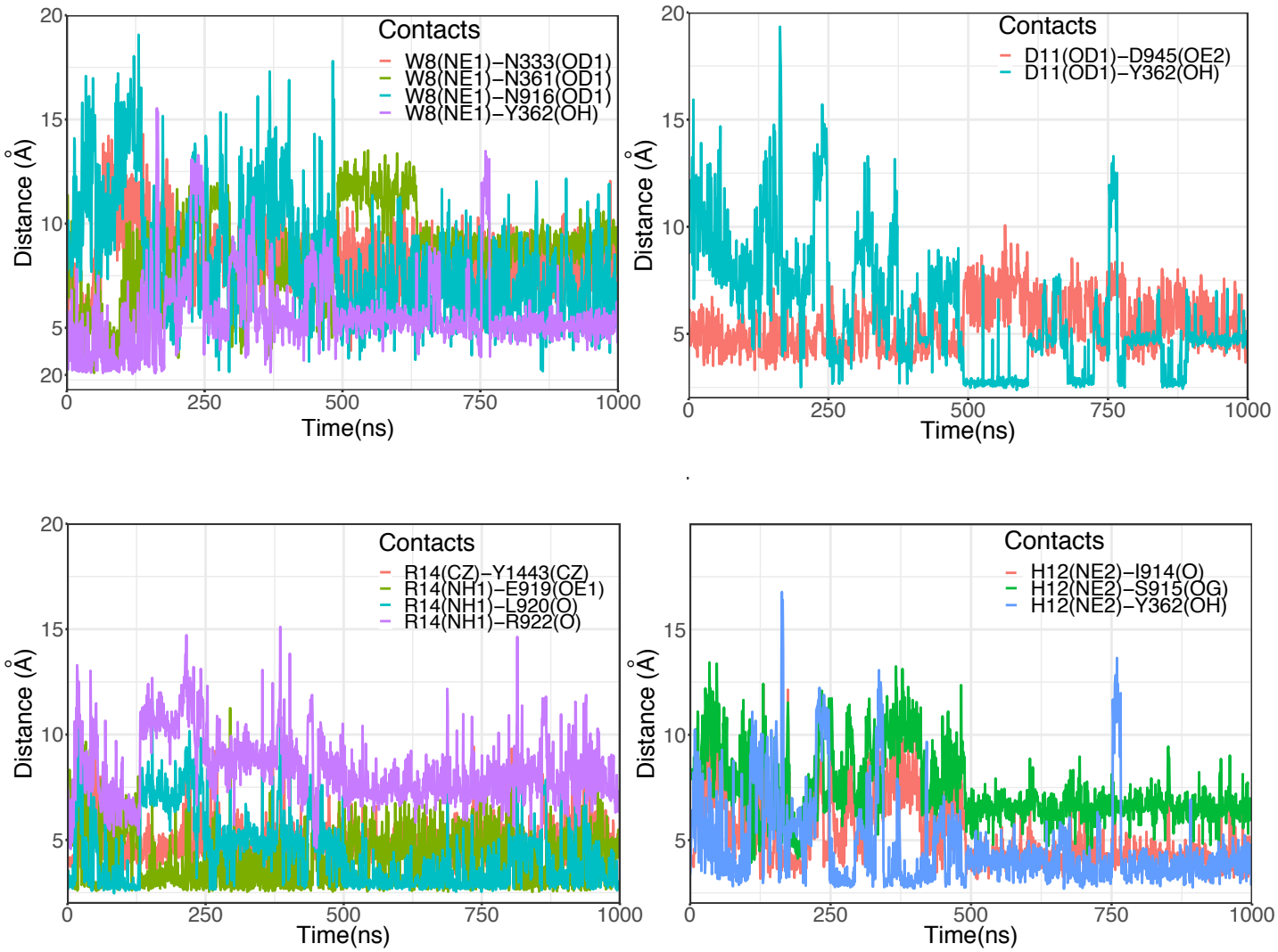
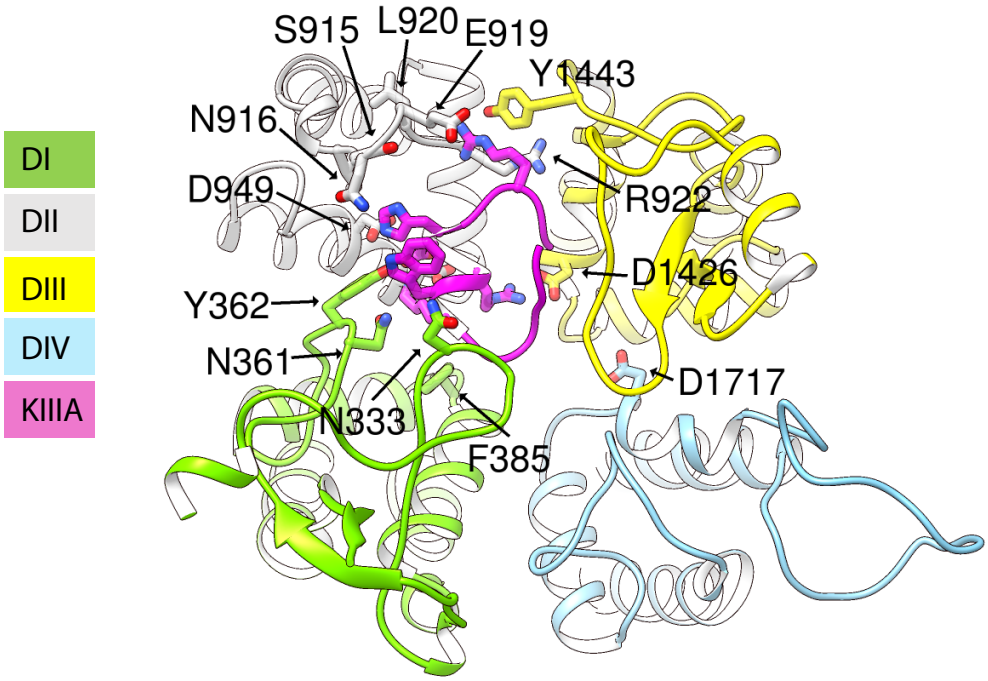
B